

AD-A124 756 INFLUENCE OF PERIODIC COMPRESSIBLE VORTICES ON LASER

1/1

BEAM INTENSITY(U) AIR FORCE INST OF TECH

WRIGHT-PATTERSON AFB OH SCHOOL OF ENGINEERING

UNCLASSIFIED C P WESTON DEC 82 AFIT/GRE/AA/82D-32

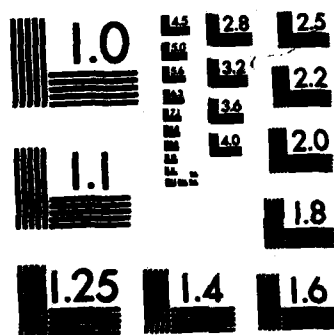
F/G 20/5

NL

END

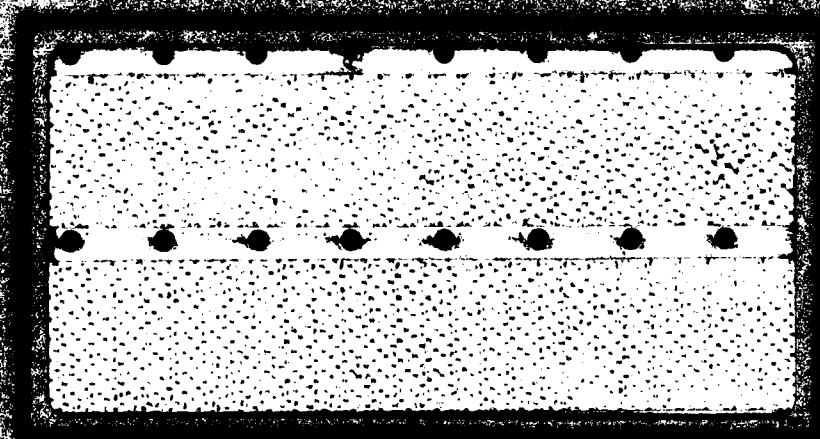
FILED

bvic



MICROCOPY RESOLUTION TEST CHART
NATIONAL BUREAU OF STANDARDS-1963-A

AD A124756



DTIC
ELECTE
FEB 12 1961

DEPARTMENT OF THE AIR FORCE
RESEARCH AND DEVELOPMENT (AR&D)

AIR FORCE INSTITUTE OF TECHNOLOGY

Wright-Patterson Air Force Base, Ohio

88 02 022 075

AFIT/GAE/AA/82D-32

INFLUENCE OF PERIODIC COMPRESSIBLE
VORTICES ON LASER BEAM INTENSITY

THESIS

AFIT/GAE/AA/82D-32

Craig P. Weston
Captain USAF

DTIC
ELECTE
FEB 22 1983
S E D

Approved for public release; distribution unlimited.

INFLUENCE OF PERIODIC COMPRESSIBLE
VORTICES ON LASER BEAM INTENSITY

THESIS

Presented to the Faculty of the School of Engineering
of the Air Force Institute of Technology

Air University

in Partial Fulfillment of the

Requirements for the Degree of

Master of Science

by

Craig P. Weston, B.S.

Captain USAF

Graduate Aeronautical Engineering

December 1982

Accession For	
NTIS GRA&I	<input checked="checked" type="checkbox"/>
DTIC TAB	<input type="checkbox"/>
Unannounced	<input type="checkbox"/>
Justification	
By _____	
Distribution/	
Availability Codes	
Dist	Avail and/or Special
A	



Preface

This study is the first in a continuing AFIT research program sponsored by the Air Force Weapons Laboratory to investigate real fluid effects on laser beam propagation. The research explored the concept of generating and measuring specific bandwidths of "turbulence" and assessed the influence of the "turbulence" bandwidths on a laser beam. I hope the ideas contained in this thesis stimulate further analytical and empirical investigations in this important area known as aer-optics.

I would like to thank en masse the many individuals of the Air Force Weapons Laboratory and Wright Aeronautical Laboratories who so generously loaned me equipment and provided technical assistance. I particularly thank Maj. John A. Vonada and Dr. William C. Rose for advising me on the practical and theoretical aspects of hot wire anemometry. I wish to acknowledge the guidance and assistance of my thesis advisors, Maj(Dr.) Eric J. Jumper, Dr. William C. Elrod and Dr. Harold E. Wright. Finally, I thank my wife, Doris, and two sons, Colin and Kelly, for the sacrifices they made for this research.

Contents

	Page
Preface	ii
List of Figures	v
List of Tables	vii
List of Symbols	viii
Abstract	x
I. Introduction	1
II. Theory and Approach	3
Periodic Flow Field Creation	3
Flow Field Measurements	4
Visualization of Flow Field Structure	10
Density Variation Effect on Laser Beam Intensity	11
III. Experimental Apparatus	13
Periodic Vortex Generator	13
Mass Flux Measurement	17
Pressure Measurement	19
Schlieren Photography	21
Beam Generation and Measurement	25
IV. Experimental Procedure	28
Mass Flux Measurement	28
Pressure Measurement	30
Schlieren Photography	31
Beam Generation and Measurement	32
V. Results and Discussion of Results	35
Flow Field Character	35
Nature of the Near Field Flow	39
Significance of Beam Degradation	43
Anemometer Limitations	51
Pressure Probe Limitations	52
VI. Conclusions	54

Contents

	Page
VII. Recommendations	56
Bibliography	58
Appendix A: Derivation of Fluctuating Density from Mass Flux and Pressure Measurements	60
Appendix B: Relationship of Measured Density to Beam Intensity	63
Appendix C: Hot Film Mechanical Resonance Calculations	67
Vita	69

List of Figures

<u>Figure</u>		<u>Page</u>
1	Strouhal Coefficient as a Function of Reynolds Number	5
2	Example of Vortices Shed from a Cylinder in Compressible Flow	5
3	Examples of Autocorrelation Function Plots	8
4	Examples of Power Spectral Density Plots	9
5	Orientation of Jet Nozzle Exit, Rod Grid and Coordinate System	14
6	Largest and Smallest Diameter Rod Grids	16
7	Mass Flux System Arrangement	18
8	Hot Film, Fairing and Grid Perspective Views	20
9	Static Pressure Probe Installed in Fairing	22
10	Pressure Measurement System Arrangement	23
11	Schlieren Photography System Arrangement	24
12	Beam Degradation Measurement System Arrangement	26
13	Grid 2 Mass Flux Autocorrelation Plots for Three Lateral Offsets at 3 Rod Diameters Downstream	37
14	Grid 2 Mass Flux Power Spectral Density Plots for Three Lateral Offsets at 3 Rod Diameters Downstream	38
15	Schlieren Photograph of Grid 2 Periodic Flow at $M = .6$	40
16	Schlieren Photograph of Grid 10 Periodic Flow at $M = .6$	41
17	Schlieren Photograph of Grid 48 Periodic Flow at $M = .6$	42

List of Figures

<u>Figure</u>		<u>Page</u>
18	Grid 20 Laser Beam Vertical Broadening at Test Location 1	47
19	Grid 10 Laser Beam Steering at Test Location 1	47
20	Grid 10 Laser Beam Vertical Broadening at Test Location 2	48
21	Grid 5 Laser Beam Horizontal Broadening at Test Location 2	48
22	Jet Shearing Flow Laser Beam Vertical Broadening at Test Location 3	49
23	Grid 10 Laser Beam Broadening at Test Location 3 . . .	49
24	Grid 3 Laser Beam Horizontal Broadening at Test Location 3	50
25	Grid 2 Laser Beam Horizontal Broadening at Test Location 3	50
26	Characteristic Curve of Film Response	64

List of Tables

<u>Table</u>		<u>Page</u>
I	Rod Grid Design Parameters	17
II	Beam Degradation Measurement Test Points	33
III	Results of Beam Degradation Measurements	44

List of Symbols

<u>Symbol</u>		<u>Units</u>
A	area	cm ²
B	Gladstone-Dale constant	cm ³ /kg
C	constant, based on wavelength	1/cm
D	rod diameter	cm
E	exposure	joules/cm ²
E ₀	baseline film exposure	joules/cm ²
E _m	modulus of elasticity	kg/cm ²
I	intensity	joules/s
I _m	moment of inertia	cm ⁴
I ₀	reference intensity	joules/s
K	ratio of specific heats	---
L	boundary layer thickness	cm
M	Mach number	---
P	static pressure	kPa
P _t	total pressure	kPa
R	gas constant for air	joules/°K kg
R _t	auto correlation coefficient	---
R _{p pu}	cross correlation coefficient of fluctuating pressure and mass flux	---
Re _D	Reynolds number based on rod diameter	---
S	Strouhal coefficient	---
T	static temperature	°K

List of Symbols

<u>Symbol</u>		<u>Units</u>
T_t	total temperature	$^{\circ}\text{K}$
T_{oh}	hot wire temperature overheat ratio	---
d	film density	---
f	frequency	1/s
f_i	i mode of natural frequency	1/s
g	acceleration due to gravity	cm/s^2
l	length	cm
l_z	length of boundary layer eddies	cm
t	time	s
x	an arbitrary function	---
u	velocity	m/s
w	specific weight	kg/cm^3
γ	slope of film characteristic curve	---
λ	laser light wavelength	cm
ν	kinematic viscosity of air	m^2/s
ρ	density of air	kg/m^3
ρu	mass flux	kg/s
σ	phase aberration of laser light	---
'	fluctuating component of a quantity	---
—	mean component of a quantity	---
< >	RMS value of a quantity	---

from 4,600 to 110,000.

Abstract

This study explored the effect of narrow-band, vortex-induced density fluctuations on the beam quality of a laser propagated through the fluctuating flow. The research was a dual investigation. First, the ability to create and characterize "tailored", fluctuating flows was explored. Second, the degradation of the laser beam due to these various flows was assessed.

The flows of periodic vortices were created by cylindrical rods placed at the exit plane of a 1 cm by 10 cm rectangular free jet issuing air at $M = .6$. Reynolds number based on rod diameter varied from 4.6×10^3 to 1.1×10^5 . Mean and fluctuating mass flux, total pressure and static pressure time histories of the flows were measured in order to derive fluid eddy passage frequency, eddy length and periodic density fluctuation data. Schlieren photographs were obtained for further assessment of the flow fields.

A nominal 1 mW laser beam was propagated at two wavelengths transversely through the periodic portion of each flow. The far field beam cross-section was analyzed to determine beam intensity degradation. A Strehl ratio for each flow field was deduced from pseudo-quantitative data.

A hot film anemometer and pressure probes provided limited mass flux and pressure time history data due to mechanical resonances caused by the high frequencies and strength of eddy generation. The schlieren

photographs confirmed that distinct, periodic fluid eddies existed for at least nine rod diameters downstream of the jet exit. Each of the rod grids produced significant beam degradation but affected the beam shape differently. At 2.5 cm downstream of the jet exit, the beam degradation due to the grids was much less than the degradation due only to the jet shearing action with the still air of the test cell.

I. Introduction

A number of environmental factors affect the propagation efficiency of a high energy laser from an airborne platform through the atmosphere. A measure of propagation effectiveness is the average peak beam intensity at the target. Losses in average peak intensity may occur because of beam jitter, beam wander and general beam quality degradation. Jitter is usually attributed to mechanical vibration of the platform. Solutions may be found in exploiting solid mechanics and vibration theory. Wander is often associated with large scale density gradients in the propagation medium due to aircraft boundary layer separation and atmospheric turbulence. This is generally a low frequency problem that may be solved with beam feedback and control loops (Ref 1). One aspect of general beam quality degradation is the small, high frequency density disturbances associated with a compressible (Mach number greater than .4) turbulent boundary layer (Ref 1). It is generally understood that these density fluctuations cause index of refraction variations on a scale smaller than the beam diameter and result in average peak intensity decay as well as beam broadening. Studies of nearly isotropic turbulence (Ref 2), free jets (Ref 3) and turbulent boundary layers (Ref 4) have been partially successful in understanding this particular aero-optics phenomenon.

Since some success in restricting the band of turbulence in a boundary layer has been reported (Ref 5), it has been suggested that such a technique might be used to tailor the airborne platform boundary

layer turbulence for optimum beam-pass conditions (Ref 6). The purpose of this research was to explore the relationship between turbulence bandwidth and average peak beam intensity. However, it was not evident that bandwidths of "turbulence" could be created and quantified or that the effect on a laser beam could be adequately measured.

From this background, four research objectives were developed.

1. Create, under controlled conditions, a number of compressible flow fields with a narrow bandwidth of "turbulence" of distinct fluid eddy sizes and passage frequencies in each flow.
2. Deduce density fluctuations in the periodic flow fields from fluctuating mass flux and pressure measurements of the fields.
3. Determine the flow fields' periodicity as well as eddy growth and mixing from schlieren photographs of the fields.
4. Propagate a low power laser beam at selected wavelengths through the periodic density fluctuations of the flow fields in order to assess the relationship of eddy size, eddy passage frequency and laser wavelength to beam peak intensity degradation.

The remainder of the report describes the methods used to achieve the objectives and the results of the research. The next section of the report presents the theoretical approach and is followed by sections discussing the experimental apparatus and procedure. Subsequent sections detail the results and conclusions of the research while a final section suggests areas for further investigation.

II. Theory and Approach

Prior to the design of any experimental apparatus, the theory for creating a flow with periodic density fluctuations, measuring its periodicity and assessing its influence on laser beam intensity was extensively researched. The practical implementation of the theory was constrained to the use of a readily available, well documented, rectangular free jet (Ref 7 and Ref 8). Since the investigation of the research objectives evolved in steps from flow field creation to beam degradation measurements, their theoretical approaches are presented in that order.

Periodic Flow Field Creation

The decay of a flow field initially dominated by fluid vortices or eddies created from cylindrical rods was extensively investigated by Roshko (Ref 9). His work produced two results of interest to this research. One result was that for Reynolds number based on cylinder diameter, Re_D , from 300 to 1×10^4 , a predominant eddy shedding frequency was evident for at least 24 cylinder diameters downstream of the vortex generator. However, the shedding energy decay was rapid. For example, at $Re_D = 4 \times 10^3$, at 6 diameters downstream of the vortex generator the ratio of periodic to random fluctuating kinetic energy was 7/3 while at 24 diameters the ratio was 1/9. The other result was the determination of Strouhal coefficients for the 300 to 1×10^4 Re_D range from shedding frequency measurements (Ref 9: 810-814) through the relationship

$$S = \frac{f D}{u} \quad (1)$$

Schlichting subsequently compiled the results of many research studies to provide Strouhal coefficients to the point of vortex flow instability, $Re_D = 2 \times 10^5$, and beyond (Ref 10: 31-33). The coefficients are presented in Fig. 1. Roshko's research and the Strouhal relationship was the theoretical basis for creating and predicting a periodic flow field similar to that shown in Fig. 2 for a single cylinder in a flow duct.

From a practical standpoint, the eddies were created by vertical grids of cylindrical rods mounted in frames and placed at the jet exit plane with an orientation normal to the flow. A jet exit Mach number, M , of .6 was chosen so that compressible eddies were formed, with attendant density variations, to influence the laser beam. Since jet exit Mach number is a function of chamber pressure, exit atmospheric pressure and exit area (see Eq. 7, Section IV), the rod grids were sized to present a constant area restriction of the jet exit plane. In this manner a constant exit Mach number at the throats formed by the rods was maintained. Hence, as rod size decreased the number of rods per grid increased. Rod diameters were selected to give a wide range of Re_D which produced greater than an order of magnitude of expected eddy shedding frequencies (see Section III). Thus, the laser beam was subjected to a range of eddies characteristic of the various rod diameters and their associated Strouhal shedding frequencies.

Flow Field Measurements

Laser beam degradation in the periodic flow fields would be a result of index of refraction variations caused by density fluctuations in the flow. Hence, any theory that related the dependence of beam degradation to eddy size and frequency required fluctuating density data

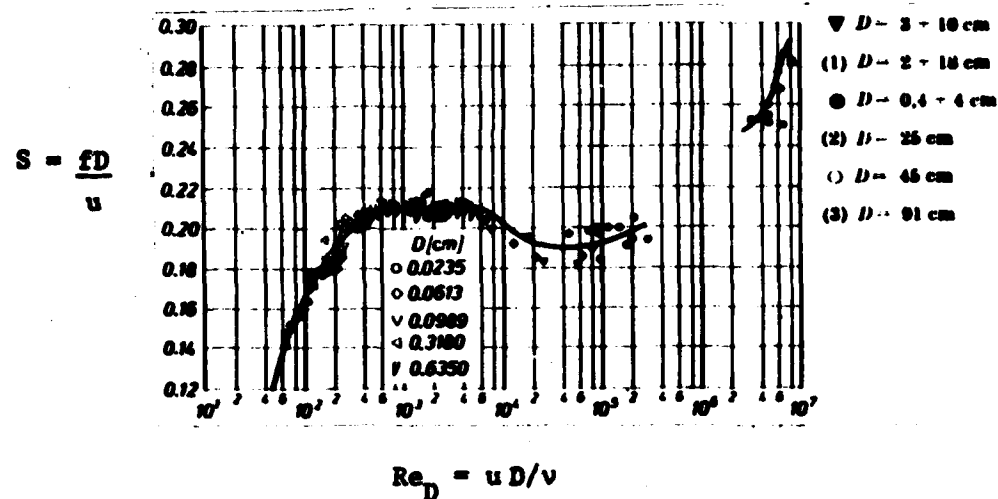


Figure 1. Strouhal Coefficient as a Function of Reynolds Number (Ref 10: 32)

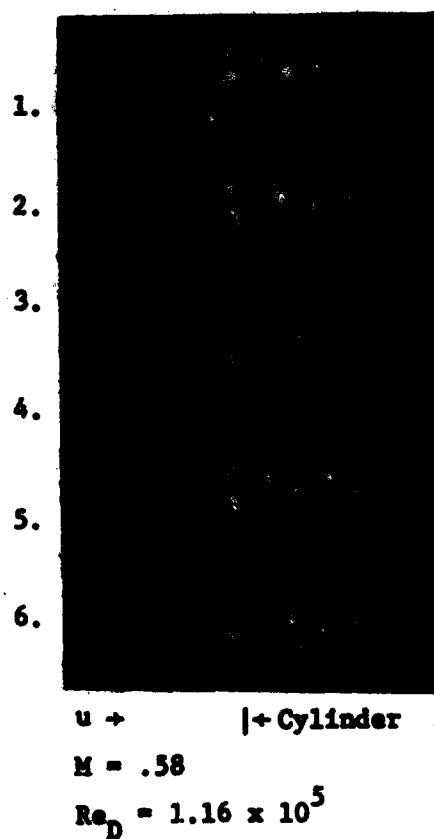


Figure 2. Example of Vortices Shed from a Cylinder in Compressible Flow (Ref 11: 283)

as a parameter. Density variations in a flow cannot be measured but must be deduced from temperature, pressure and mass flux measurements of the flow field. Rose (Ref 12: 20-23) has shown that in the absence of total temperature, T_t , changes, density fluctuations can be related to mass flux and pressure measurements by

$$[1 + (K-1)M^2]^2 \frac{\overline{\rho'^2}}{\bar{\rho}^2} = \frac{(\overline{P'})^2}{(\bar{P})^2} + [(K-1)M^2]^2 \frac{[\overline{(\rho u)'}^2]}{(\bar{\rho} u)^2} \quad (2)$$

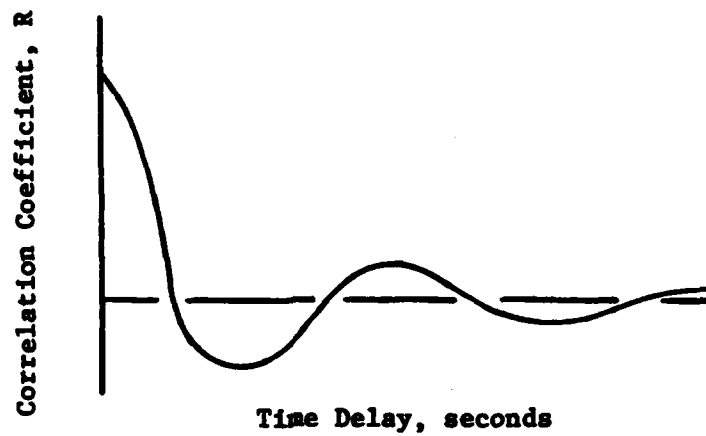
Appendix A details the derivation of Eq. 2 from the equation of state and isentropic flow relations. Thus, if mean and fluctuating static pressure and mass flux as well as mean density of the periodic flow fields were measured then the fluctuating density could be deduced from Eq. 2. A hot wire anemometer and pressure probe provided the necessary data.

The single hot wire probe was aligned parallel to the grid rods so it could traverse across and downstream of the jet exit to measure mean and fluctuating mass flux at precise locations in the flow fields. Probing the flow at two separate wire temperature overheat ratios, T_{oh} , with no difference in the two mass flux measurements verified the absence of T_t fluctuations (Ref 13: 398). It was then valid to use Eq. 2 to deduce density fluctuations. The fluctuating mass flux hot wire signal was processed by an on-line autocorrelator and frequency spectrum display to analyze the flow for periodicity. The autocorrelation function of a signal, $R(\Delta t)$, is a comparison of the signal's time-delayed value with its initial value

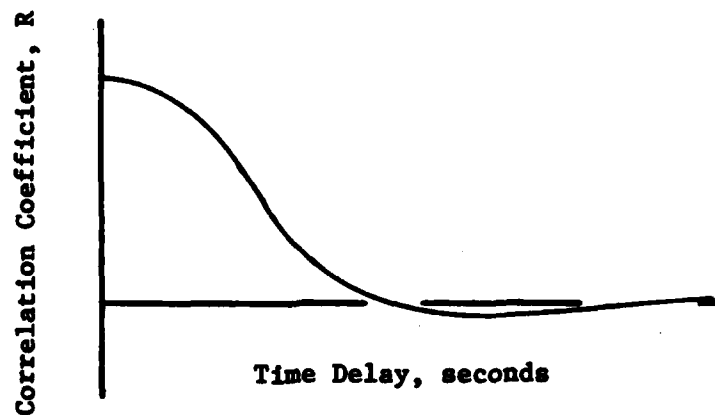
$$R_t(\Delta t) = \lim_{t \rightarrow \infty} \frac{1}{t} \int_0^{t+\Delta t} x(t)x(t+\Delta t)dt \quad (3)$$

The autocorrelation plot for a periodic mass flux signal in wideband turbulence is similar to Fig. 3A while the plot for generalized turbulence appears like that of Fig. 3B (Ref 14: 19-20). Additionally, the characteristic eddy passage time and length, the integral scales, of the largest eddies in the flow can be determined manually from the autocorrelation plot (Ref 15: 36-42). The spectrum display performed the electronic equivalent of the Fourier transform of the autocorrelation function to provide a power spectral density (PSD) plot to display relative energy (mass flux signal squared) versus frequency (Ref 14: 23, 79-81). A PSD plot for a strongly periodic flow appears similar to Fig. 4A while that for generalized turbulence might appear similar to Fig. 4B (Ref 14: 22-24). The anemometer, correlator and spectrum display provided mass flux data as well as a qualitative assessment and cross-check of its periodicity.

Mean and fluctuating pressure data was obtained with high frequency response, piezoresistive transducers mounted in total and static pressure probes. The design of the probes was patterned after those successfully used in another study (Ref 16). The fluctuating pressure signal was also processed by the autocorrelator and spectrum display to determine its periodicity and frequency content. Once the mean and fluctuating pressure and mass flux data for a flow was obtained, the mean density was determined from the equation of state. These parameters could then be substituted into Eq. 2 to provide the fluctuating component of density at each point in the flow field. The frequency of density fluctuation and a characteristic eddy length could be deduced from autocorrelation and PSD measurements at the corresponding point in the flow. This information would be available for use in any analytical work to

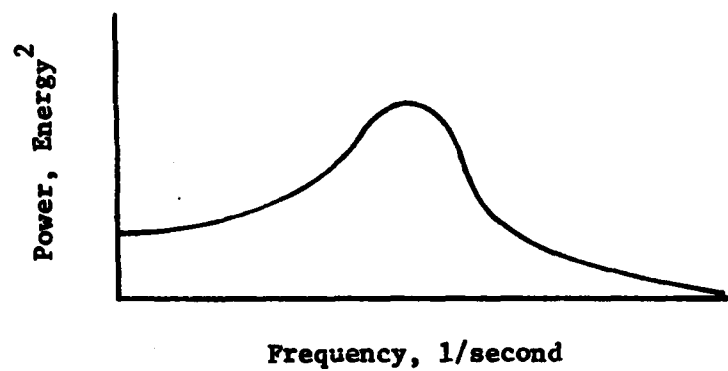


A. Periodic Signal with Wideband Turbulence (After Ref 14:20)

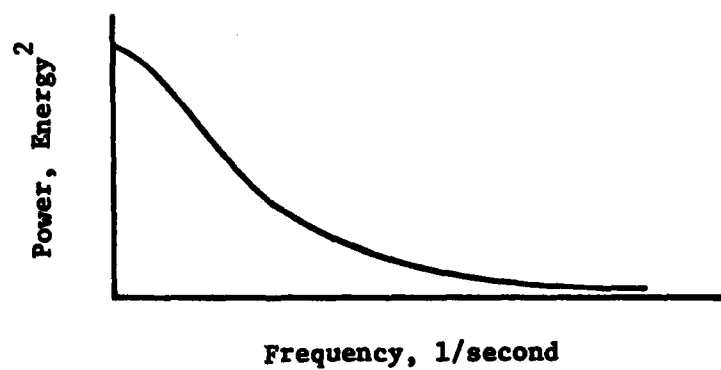


B. Wideband Turbulence (After Ref 15: 150)

Figure 3. Examples of Autocorrelation Function Plots



A. Periodic Signal with Wideband Turbulence (After Ref 14:24)



B. Wideband Turbulence (After Ref 15:203)

Figure 4. Examples of Power Spectral Density Plots

predict laser beam sensitivity to density fluctuation magnitude, length and frequency. While density variations at discrete locations were inferred from these measurement processes, schlieren photographs provided a global, qualitative assessment of the density variations in the flow field at any instant.

Visualization of Flow Field Structure

Density gradients in the flow fields were recorded by means of Toepler-schlieren photography. In general use, the test section is illuminated with nearly collimated light expanded from an intense, point light source. On the opposite side of the test section the light is refocused to a point and a knife edge is placed to partially block the subsequent expansion of the light into a camera lens. Density gradients in the test section cause index of refraction changes which refocus the nearly parallel light rays to points either above or below the knife edge, which causes some portions of the test section to appear brighter or dimmer than others. A photograph of the light traversing the test section and knife edge provides a map of the density gradients in the test section at that instant (Ref 17: 65-67). A spark lamp, high speed film and large mirrors oriented perpendicular to the axis of the grid rods provided the best resolution of the eddies across the flow field and for about 15 cm downstream of the jet exit. The photographs were used to quantify density eddy length, identify eddy mixing zones and, by use of Eq. 1, confirm the shedding frequency measurements of the anemometer and pressure probes. The density variations that caused the density gradients recorded by schlieren photography were the same variations that would affect the laser beam intensity in the far field.

Density Variation Effect on Laser Beam Intensity

A simple measure of beam degradation is the Strehl ratio, I/I_0 , where I is the degraded beam intensity and I_0 is the beam intensity at the source or other reference point. The index of refraction changes caused by turbulent boundary layers depend on the laser light wavelength, λ , and density eddy size, l_z . A formula that has been used with some success in predicting beam degradation through a turbulent boundary layer is:

$$\frac{I}{I_0} = \exp(-C^2 \sigma^2) \quad (4)$$

where

$$C^2 = \frac{2\pi}{\lambda} \quad (5)$$

$$\sigma^2 = \sqrt{\pi} B^2 \int_0^L (\overline{\rho'})^2 l_z dz \quad (6)$$

and B is the Gladstone-Dale constant while L is the thickness of the boundary layer. The Gladstone-Dale constant is also dependent on laser light wavelength (Ref 4: 155). The Strehl ratio dependence on laser wavelength and density eddy length is apparent in Eq. 4. It is also known that beam intensity degradation due to beam wander tends to be caused by large density eddies the size of the beam diameter which act as a single lens to steer the entire beam away from its original propagation direction. Beam intensity is also attenuated by many random eddies much smaller than the beam diameter. They act as a multitude of minute lenses which steer small portions of the beam in a multitude of directions (Ref 1). Actual measurements of far field Strehl ratios for a laser beam propagated at several wavelengths through the periodic flows might provide some linkage between previous observations and

analytical relationships. Any correlation between laser wavelength and turbulence density eddy size and passage frequency might become evident.

The experimental approach to beam degradation measurements was similar to that used in an earlier investigation (Ref 3: 33-40). Laser beams of different wavelengths were propagated across the jet at the point of optimum flow periodicity in a plane parallel to the grid rods. The refracted laser light caused distortions across the beam wavefront which would not become apparent until many meters past the flow, in the far field. The far field effect was simulated over a shorter distance by an optical transformation to the far field. A large collector lens was placed just past the flow to refocus the light to a point image. Since the beam degradation and distortion were present but not readily discernable at the focal point, a small lens placed at the focal point re-expanded the beam for analysis. This arrangement apparently compressed the effect of beam scatter and attenuation over the many meters to travel to the far field into a distance of several meters.

Photographs of the undisturbed and periodically disturbed beam projected on a translucent surface were analyzed with a densitometer. The two density maps were converted to relative beam intensity maps by the method (Ref 18: 162, 179-180) described in Appendix B, and compared in a Strehl ratio. Plotting the intensity cross-section allowed beam shape broadening and total energy loss to be calculated. Additionally, a three-dimensional image analyzer was used to convert image intensity to a vertical relief map of the beam intensity shape. Hence, a pseudo-quantitative assessment of the effect of the flows was possible.

III. Experimental Apparatus

The experimental apparatus consisted of a free jet with various rod grids, an electronic system to measure and analyze the flow fields, a schlieren photography system for flow visualization and a laser beam generation and analysis system for studying the aero-optic interactions. Since only one system was used with the jet at one time, the jet and each system are independently described.

Periodic Vortex Generator

Flow fields with periodic vortices were created by grids of cylindrical rods placed at the exit of a 1 cm by 10 cm rectangular free jet. The free jet flow field at various Mach numbers was thoroughly investigated in previous studies (Ref 7 and Ref 8). These studies documented the good two-dimensional qualities and less than .3% turbulence of the jet at the exit plane (Ref 7: 24). Hence, the jet was an ideal source for two-dimensional eddy generation. For this study, the jet internal heaters and steel shot heat conductor bed which had been used in the previous studies were removed. The jet nozzle exit long dimension was placed parallel to the test cell floor with the orientation of grid plates and coordinate system as depicted in Fig. 5. A 3000 kg optical table was placed approximately 57 cm below and parallel to the X-Y plane of the nozzle exit. The table provided a steady reference surface for hardware placed at the jet exit. Located on the table was a Gaernter Scientific Co. cathetometer. The cathetometer, with a three-dimensional

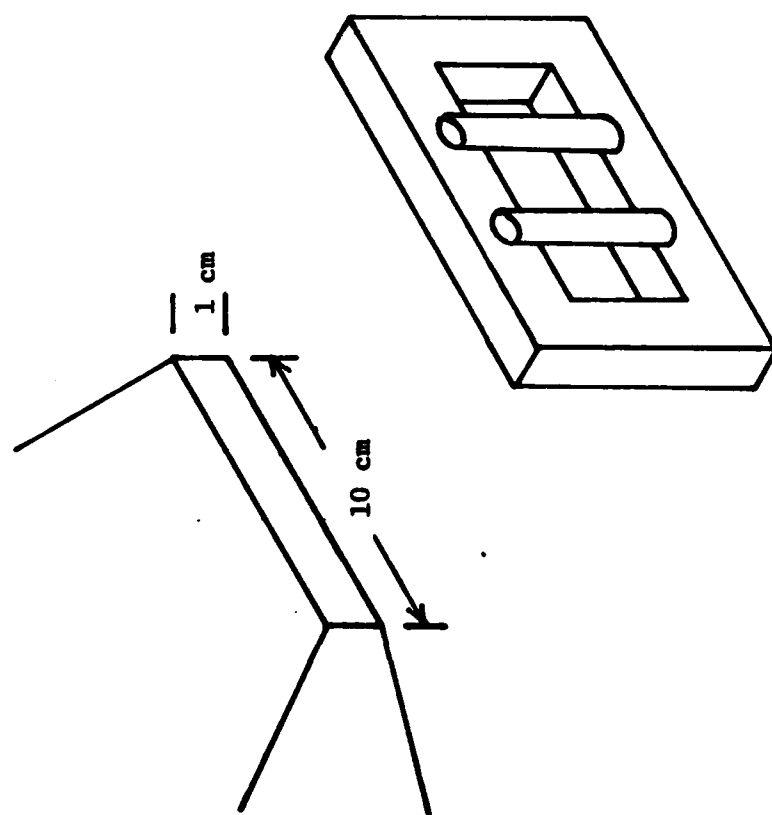


Figure 5. Orientation of Jet Nozzle Exit, Rod Grid and Coordinate System

positioning accuracy of $\pm .005$ cm, was used as a support mechanism for the anemometer hot film and pressure probes. A 76 cm mercury manometer and a mercury thermometer were used to measure effective total pressure and temperature in the jet stilling chamber. Because the object of the jet apparatus was to generate two-dimensional vortices of specific bandwidths of eddy size and passage frequency, the design of the rod grids was crucial.

The grids of cylindrical rods were fastened to plates which framed the cylinders. These plates were compatible with a common mounting block welded to the nozzle cone in a manner that allowed the nozzle exit plane to protrude from it. The rod grid plates were individually attached to the block so that the rods were parallel to the jet Y-Z plane and nearly touched the nozzle exit. Seven cylinder diameters were chosen, based on predictions made using Eq. 1 and Fig. 1, to form the maximum practical parameter range for the study. Table I lists these seven grids as well as their associated Re_D and expected shedding frequency. The largest cylinder diameter was restricted by the Re_D upper limit of stable vortex flows (Ref Fig. 1) while the smallest diameter was chosen to preclude shedding frequencies higher than the resolution ability of the anemometer. The two extreme rod diameters were the end points of a bandwidth of more than one order of magnitude of expected vortex shedding frequencies. The relative size of the two rods is apparent in Fig. 6. Diameters chosen for the intermediate rods were constrained by the requirement for 6 diameter spacing of rod axial centerlines. Previous research (Ref 9: 809 and Ref 19: 29-37) implied this lateral spacing would preclude vortex mixing

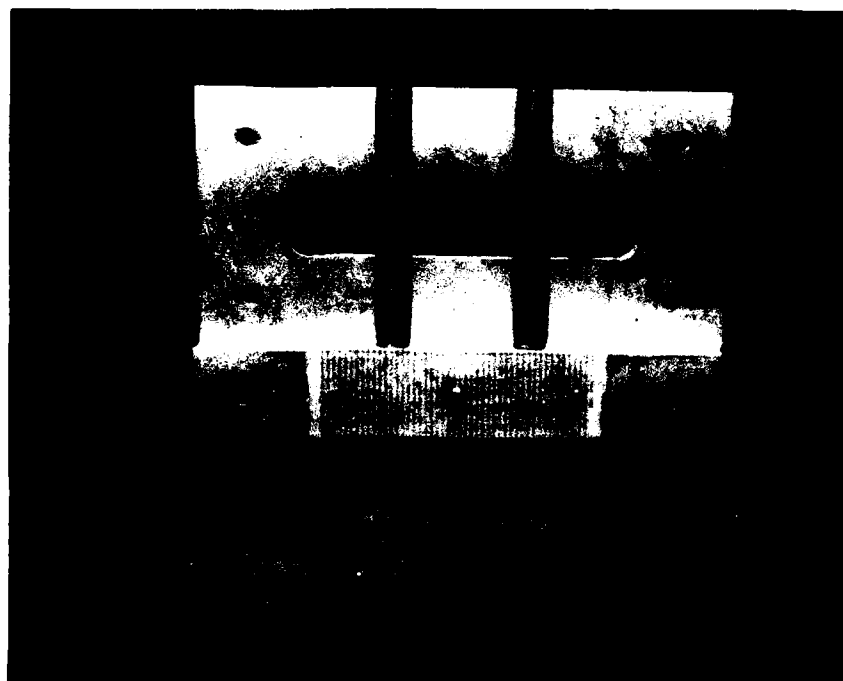


Figure 6. Largest and Smallest Diameter Rod Grids

TABLE I

Rod Grid Design Parameters

Grid number	Rod diameter (cm)	Rods per grid	Re_D ($\times 10^3$)	S (Ref Fig. 1)	f (kHz)
2	.794	2	110.0	.195	5.1
3	.528	3	73.3	.193	7.6
4	.396	4	55.0	.190	9.9
5	.318	5	44.0	.190	12.3
10	.159	10	22.0	.190	24.7
20	.079	20	11.0	.195	50.7
48	.033	48	4.6	.210	130.0

for at least 6 diameters downstream. This consideration, plus the constraint of constant rod area obstruction of the nozzle exit, limited rod diameter selection to those that met a 6 diameter spacing with a whole numbers of rods. Once sized, the rod grids were manufactured in a precision process that insured rod diameter uniformity and spacing to within $\pm .005$ cm.

Mass Flux Measurement

The anemometer is a well documented, universally accepted flow investigation tool requiring no detailed theoretical description. It was used to measure the mass flux time history of the jet flow fluctuations. The general system arrangement is depicted in Fig. 7. In brief, a single Thermo-Systems, Inc. (TSI) 1214-10 .003 cm diameter hot film was oriented parallel to the jet Z axis (i.e., parallel to the grid rods) and was supported by an elbow holder in the X-Z plane. The elbow holder was attached to the cathetometer L shaped arm which allowed the

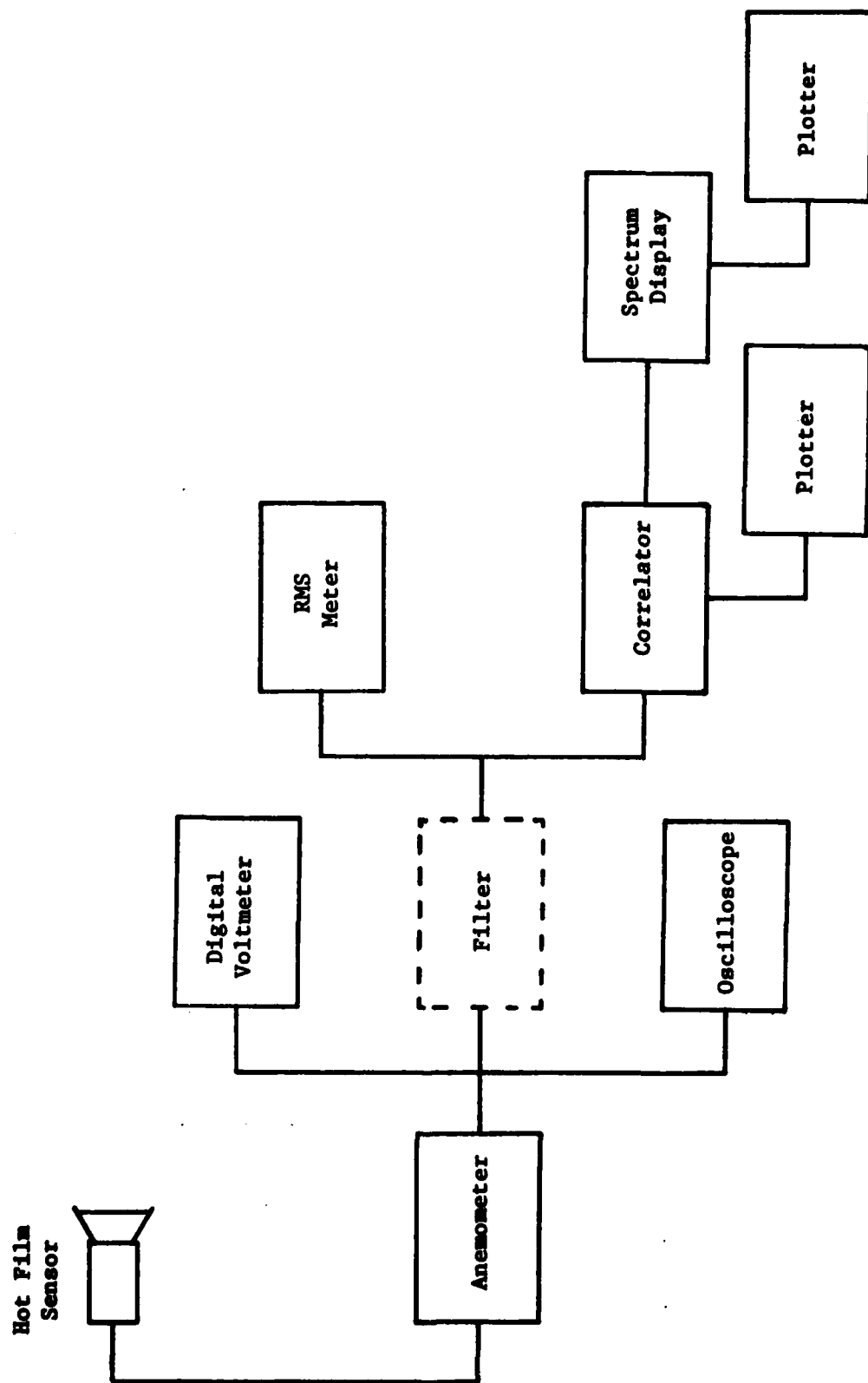


Figure 7. Mass Flux System Arrangement

cathetometer to be placed to one side of the jet flow. The hot film sensor was used in the constant temperature mode with a TSI Model 1050 anemometer. A Hewlett-Packard (HP) 3400A RMS voltmeter and an HP 34740A digital voltmeter were used to measure the fluctuating and mean voltage signal of the anemometer. The fluctuating signal was displayed on a Tektronic 465M oscilloscope to give a visual presentation of the turbulence level. The anemometer signal was also electronically processed to provide an autocorrelation function display by an HP 3721A correlator. The autocorrelation information was subsequently transformed into a power spectral density (PSD) plot display by an HP 3720A spectrum display. The autocorrelation and PSD plots were permanently recorded by two HP 7045B plotters.

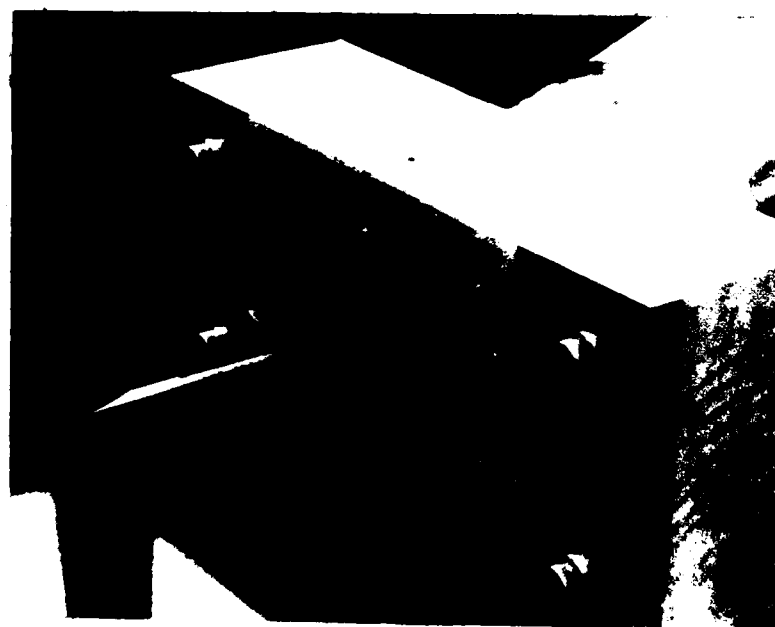
In the early stages of the flow measurement work two additions were made to the system. A fairing for the hot film elbow support was attached to the cathetometer arm to preclude flow induced vibration of the 15 cm vertical (Z axis) length of the elbow. The final sensor arrangement, in close proximity to a grid, can be seen in Fig. 8. Another addition was the use of a General Radio Corp. Type 1952 universal filter to low pass filter the fluctuating anemometer signal so only data below 17 kHz entered the HP 3400A RMS meter and the instrumentation beyond it. This addition was required because of high level resonance signals in the 22 kHz and higher frequency range which appeared to be extraneous to the actual data. The matter is discussed in detail in Section V.

Pressure Measurement

The static and total pressure measurements were recorded and



A. View Along Y Axis



B. View Into Nozzle Exit

Figure 8. Hot Film, Fairing and Grid Perspective Views

analyzed with much of the same equipment as for mass flux measurements. Endevco 8506-5 5 kPa piezoresistive pressure transducers were mounted separately in total and static probes patterned after those used in another research effort (Ref 16). The static probe sense port was located four probe diameters aft of the probe nose and four-tenths of the fairing chord length forward of the cathetometer fairing leading edge, as shown in Fig. 9. The sensing cavity was sized to theoretically provide a Helmholtz (acoustic) resonance of about 20 kHz and an organ pipe (standing wave) resonance of 54 kHz (Ref 20: 23). The total pressure probe port projected one-half fairing chord length forward of the leading edge and was sized for a Helmholtz resonance of about 20 kHz and organ pipe resonance of 47.8 kHz (Ref 21: 355-357). The probes were singly mounted as a forward extension of the fairing chord line. The only other significant departures from the mass flux measurement system was the use of a Power Mate Corp. 10 volt regulated DC power supply and a Honeywell A20B-34 amplifier, in place of the anemometer, to power the transducer bridge and amplify its output signal. The general system arrangement is shown schematically in Fig. 10.

Schlieren Photography

The Toeplier-schlieren system arrangement is presented in Fig. 11. In order to eliminate a number of turning mirrors, the free jet nozzle was rotated to align its short dimension or X-Z plane parallel to the optical table. A Cook Electric Co. spark lamp, with a spark duration of less than one microsecond, provided illumination. Its spark gap was placed at the 112 cm focal length of the 19 cm diameter transmitter mirror. The transmitter mirror was aligned to project the short dura-



Figure 9. Static Pressure Probe Installed in Fairing

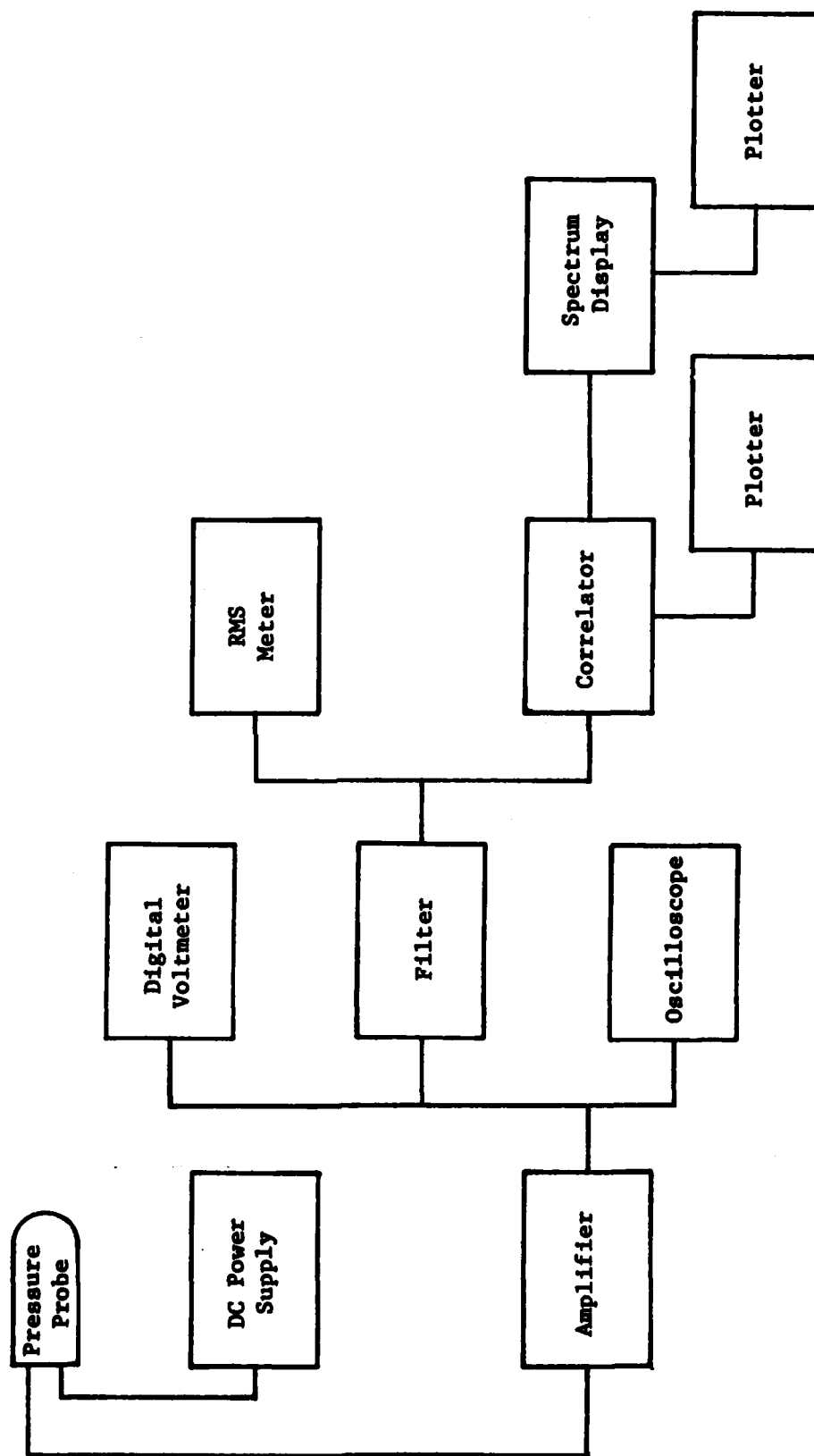


Figure 10. Pressure Measurement System Arrangement

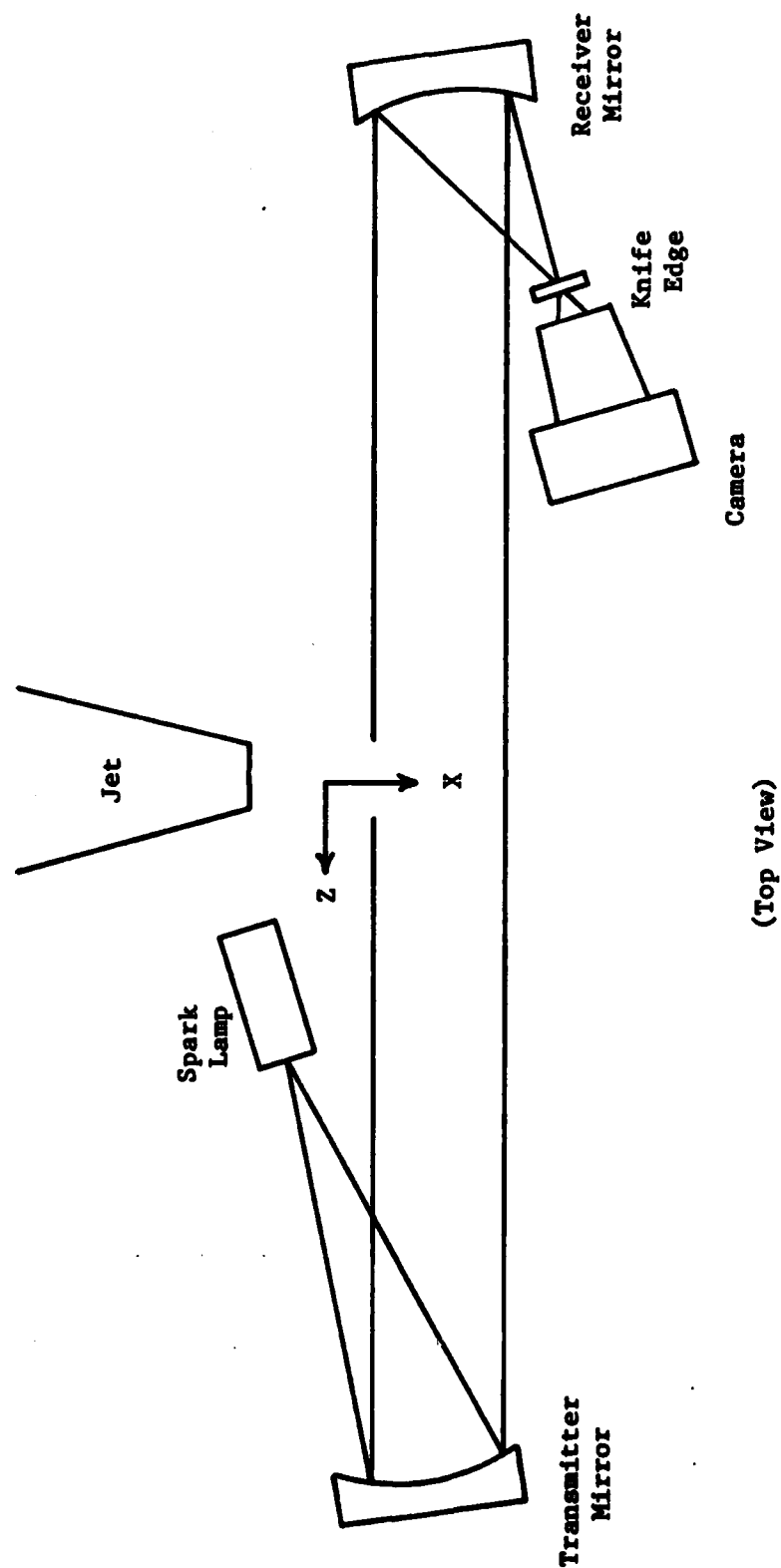


Figure 11. Schlieren Photography System Arrangement

tion, collimated light of the spark lamp perpendicular to and through the jet exit path. The 18.5 cm diameter receiver mirror was positioned approximately 4.6 m away from the transmitter mirror. A simple box camera with a knife edge aperture was placed slightly off-axis of the receiver mirror with the knife edge at the 102 cm focal point of the mirror. The camera distance from the knife edge was adjusted to place the camera film plane in focus with the test section plane. Polaroid Type 57, ASA 3000 film was used.

Beam Generation and Measurement

The far field beam discussed in Section II was effectively created with a system similar to that used in a previous study (Ref 3) and is depicted in Fig. 12. All beam generation and measurement components were mounted to optical rails which were in turn bolted to the optical table. The jet nozzle exit was aligned with its long dimension or X-Y plane parallel to the optical table. The laser and its ancillary beam conditioning equipment was placed to one side of the jet so the beam propagated along the centerline of the jet exit in the Z direction. Laser beams were generated at two wavelengths, .458 and .515 microns, by a Spectra Physics 165 Argon filled laser. A Spectra Physics 333 collimator and 332 expanding lens with an additional precision aperture produced a nominal 1 mW, 7.6 mm diameter, smooth Gaussian shaped beam. On the opposite side of the jet flow, a 10 cm diameter Zeiss Apo-Planar lens with a nominal 105 cm focal length was mounted to collect the degraded beam. A 100 cm tube connected to the rear of the lens prevented undesired additional beam degradation from extraneous air movement in the test cell. A JEA 20 power, 4.5 mm diameter microscope

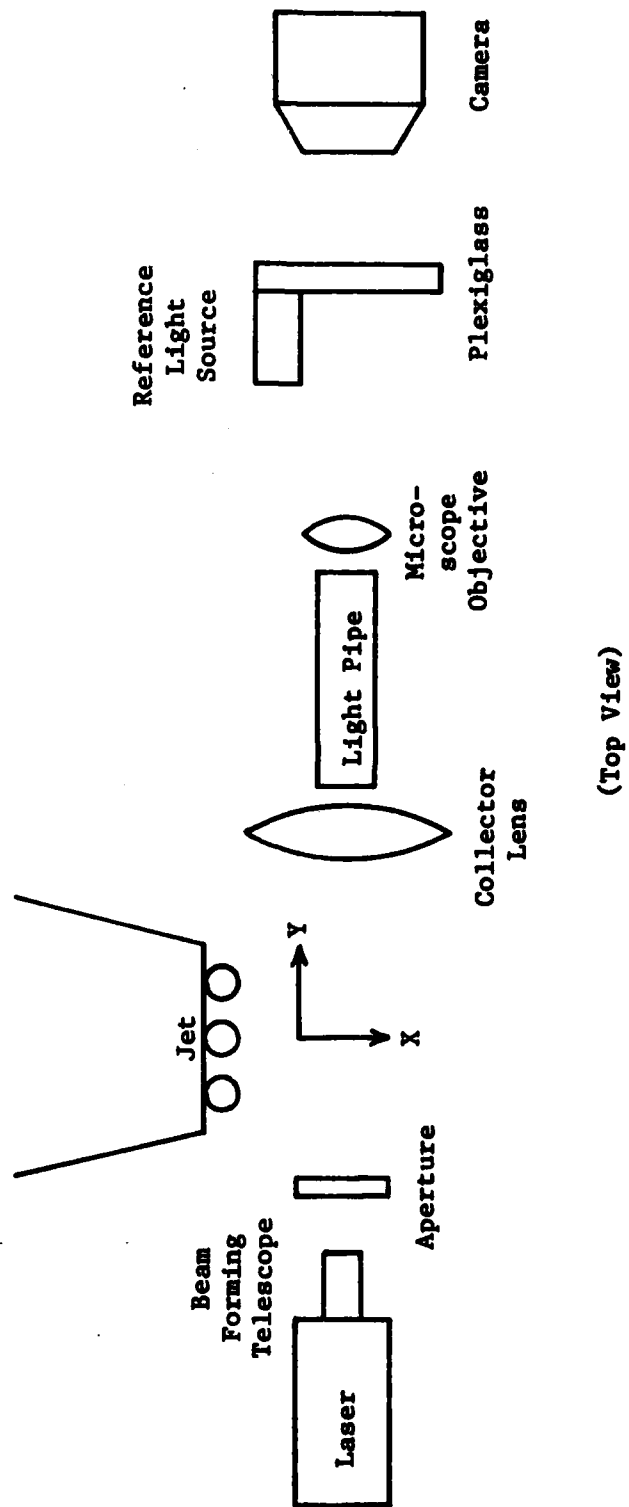


Figure 12. Beam Degradation Measurement System Arrangement

objective was placed at the focal point of the Zeiss lens in order to expand the far field beam image to approximately 15 mm diameter onto a 15 cm by 25 cm translucent piece of plexiglass. A low intensity microscope backlight was placed flush with the plexiglass surface to provide a constant intensity reference spot. The diffuse beam image and reference light spot were photographed from the opposite side of the plexiglass with a Graflex camera using Polaroid Type 55, ASA 50 positive/negative film.

The photographic negatives of the laser beam image were analyzed for relative density by an X-Rite Co. 301 densitometer with a 1 mm aperture. Additionally, three-dimensional relief maps of the beam shape and intensity profile were produced from the film using an Interpretation Systems Inc. VP-8 Image Analyzer.

IV. Experimental Procedure

A careful procedure of calibration, alignment, and trial data-gathering runs was followed for each measurement system used. The final data more accurately represented the true effect of the test conditions because many system biases and external errors were eliminated through this procedure.

Mass Flux Measurement

The single hot film sensor was first calibrated in an apparatus similar to the TSI 1125 calibrator using the procedure described in Ref 7 and Ref 8. A computer program performed a least squares curve fit of the chamber exit velocity and corresponding hot film voltage data to produce a 1% error, voltage-versus-velocity curve. After mounting the hot film in its elbow holder and fairing, a transparent plexiglass target was inserted in the jet nozzle exit. Crosshairs delineating the vertical and horizontal centerlines of the jet exit were etched on the target surface. Theodolites were placed along the X and Y axes of the jet to align the hot film probe in three dimensions with respect to the target crosshairs juncture. Once aligned, the cathetometer scale readings were recorded as the zero reference position for all traverses with that probe installation. Each time the hot film was replaced the system was realigned.

Velocity in the free jet stilling chamber was so small as to be negligible, so that chamber pressure and temperature were taken to be total conditions. These properties were then used to calculate the

average jet exit velocity from the well-known, isentropic flow relationship

$$\bar{u} = \left[2 R \bar{T}_t \left(\frac{K}{K-1} \right) \left(1 - \left(\frac{\bar{P}}{\bar{P}_t} \right)^{\frac{K-1}{K}} \right) \right]^{1/2} \quad (7)$$

After suitable manipulation this equation was solved for the \bar{P}_t required for the desired $M = .6$ exit velocity. Total pressure and temperature of the chamber were noted for each test point to insure a consistent exit velocity. A computer program used the calibration curve polynomial coefficients, mass flux voltage, T_t , P_t and Eq. 7 to provide mean and fluctuating mass flux, turbulence intensity ($(\overline{(\rho u)'}/\overline{\rho u})$), and chamber exit velocity. Equation 7 as well as the entire hot film calibration and data reduction scheme were jointly validated when jet exit velocities calculated from Eq. 7 and hot film measurements at the jet exit agreed to within 2% for preliminary jet runs. Additional runs confirmed the previously reported (Ref 7: 24) axial symmetry, tophat core velocity profile in the X direction and low turbulence of the free jet. Jet runs with representative grids 2, 10 and 48 indicated the grid generated flows were axially symmetric and mass flux measurements to within 2% for two temperature overheats, T_{oh} , implied T_t fluctuations were negligible (see Section II).

Once the baseline jet runs were accomplished, the grid generated flows were probed from 1 1/2 to 15 rod diameters downstream of the grids and laterally in one-half rod diameter increments from jet axial centerline to the edge of the flow. Mass flux data, autocorrelations and PSDs were recorded at each test point.

Pressure Measurement

The pressure transducers were statically calibrated in a test fixture that connected a compressed air source, a 150 cm water manometer and the transducers together. The Power Mate DC power supply and Honeywell amplifier were used to produce a calibration curve of the amplified transducer output. A linear curve fit of less than 2% error was consistently obtained. The transducers were then mounted in the total and static pressure probes, which were individually attached to the cathetometer fairing as needed. The probe was aligned to the jet exit in the same manner as the hot film probes. Initial jet runs at 90, 150 and 200 m/s confirmed the calibration of the total pressure probe while an increasingly larger pressure bias for increased velocity was noted for the static pressure probe. This repeatable bias was probably due to misalignment of the probe with the freestream flow or from the upstream pressure disturbance of the fairing. Autocorrelation and PSD plots of the probe signals in the jet with and without grids revealed the apparent resonances for both types of probes. Total pressure probe Helmholtz and organ pipe resonances appeared to be 20 kHz and 36 kHz while those of the static probe were 17 kHz and 32.5 kHz, respectively. These compared reasonably well with the calculated frequencies discussed in Section III. Data was subsequently taken in much the same manner as for mass flux measurements except for the use of the General Radio filter to low pass frequencies less than 15 kHz. Use of the filter eliminated data runs for grids 10, 20 and 48 due to their high eddy shedding frequencies.

Schlieren Photography

Several factors that produce high-resolution schlieren photography are elimination of parallax images in the test section, best camera focus and placement of the knife edge at the vertical or horizontal focus of the receiver mirror. Parallax was effectively eliminated by aligning the mirror post centerlines with a piece of string parallel to the now rotated Z axis of the jet so the entire exit width and 15 cm of the downstream area comprised the test section. A steady light source placed near a translucent target at the camera film plane allowed the camera to be adjusted axially on its rail until best vertical and horizontal focuses of the target image were obtained on an opaque surface at the test section vertical plane. The 1.5 cm difference in the receiver mirror focuses at the knife edge was noted and referenced to the rail. Trial jet runs with grid 2 in place dictated continued use of a vertical knife edge for best eddy density resolution. The knife edge gap was adjusted by trial and error to compensate for test section illumination changes from grid to grid.

Photographs at 90 m/s with grids 2 and 48 revealed barely discernable density fluctuations, as would be expected for this nearly incompressible flow. Once photographs of each grid flow were available, the apparent eddy shedding frequency was calculated from Eq. 1. The average flow velocity was known to be 200 m/s, the Strouhal coefficients were available and the eddy density length was derived from the average of the first three or four eddies closest to the grid rods in the photographs.

Beam Generation and Measurement

Results of the hot film anemometer measurements and schlieren photographs indicated the characteristic grid shedding frequencies and eddy lengths were most distinct at 3 to 4 1/2 rod diameters downstream of the jet exit. Rather than realign the laser and beam analysis equipment seven times for the different grids, the system was aligned to the optimum location for grids 2, 4 and 10. Data was also gathered for grids 3, 5 and 20 at these respective locations since the relative downstream distance was only slightly greater. Grid 48 was tested at the grid 10 test point as the 7.6 mm diameter laser beam could not be placed closer to the grid. Representative large and small rod diameter grids were also tested at each of the three test locations. Table II is a compendium of the test locations and pertinent factors for each test point.

Alignment of the beam generation and analysis system was simplified through the use of alignment tools. The laser and its beam conditioning attachments were aligned to an index card aperture precisely positioned on the jet near side and to the crosshairs on a second index card on the far side of the jet. Centering the overlapping laser beam annulus on the near-side card provided the proper X direction spacing while centering the beam on the second card crosshairs gave proper Z and X direction alignment. Once the laser was aligned, the cards were removed and an adjustable, transparent plexiglass target was placed on the far side optical rail and aligned to the beam. The target was positioned as necessary on the rail to align both the rail and its optical components using the laser beam as a reference. The camera was

TABLE II

Beam Degradation Measurement Test Points

Test location	Grid number	Beam centerline location from grid face in rod diameters	Beam diameter size in rod diameters
1	48	21.3	23.1
	20	8.4	9.6
	10	3.5	4.8
	5	1.3	2.4
2	20	19.4	9.6
	10	9.0	4.8
	5	4.0	2.4
	4	3.0	1.9
3	48	96.7	23.1
	10	19.2	4.8
	3	5.0	1.4
	2	3.0	1.0

similarly aligned. Shutter speed was set to 1 second to achieve a time average effect of the beam motion. The camera aperture was adjusted to avoid film saturation at the fixed shutter speed.

Before each set of data runs, the undisturbed beam and the beam degradation due to the free jet itself were photographed as the reference beam intensities for Strehl ratio calculations. After each set of data runs another undisturbed beam was again photographed for repeatability. Film for each run was from the same lot number and development was timed for consistency. The intensity of the reference

light spot was checked for a consistent value on the negatives. The slope of the film characteristic curve, γ , was determined empirically as described in Appendix B. It was .432 for the .515 micron wavelength and .465 for the .458 micron wavelength. This parameter was used to convert relative negative film densities to relative beam intensities for Strehl ratio calculations. The densitometer was used to measure film densities from which peak intensities and beam broadening were determined.

V. Results and Discussion of Results

Specific bandwidths of "turbulence" or distinct fluid eddy lengths and passage frequencies were successfully created and their effect on far field laser beam intensity was observed and quantified. Although the flow fields' mass flux and static pressure parameters could not be completely measured with the anemometer and pressure probe systems, their limited characterization of the flows was confirmed and enhanced by the schlieren photography. Each measurement system contributed to an understanding of the nature of the periodic flows.

Flow Field Character

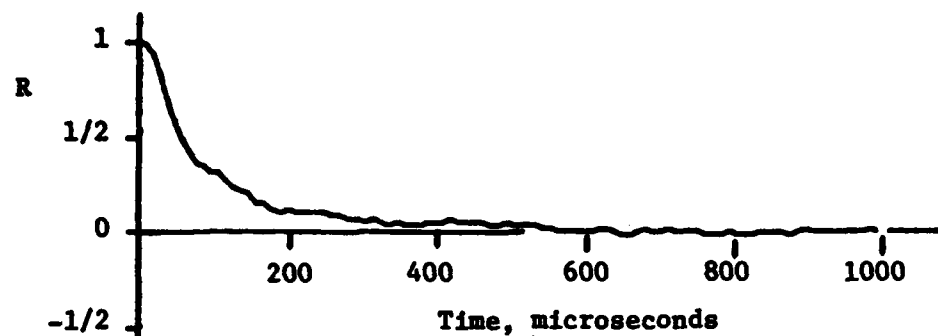
The hot wire anemometer and pressure probes were of limited use in the strongly periodic flows due to hot film mechanical resonances and probe size, respectively. The inadequacies of the two systems are more fully explained in separate discussions (see Anemometer Limitations and Pressure Probe Limitations). Because of their limitations, only flows with grids 2 through 5 could be adequately measured at $M = .6$. Even so, significant results and trends were noted at $M = .6$ and lower jet exit velocities. In general, the trends detected with the anemometer were confirmed by the pressure probes but the pressure probes had less flow field location resolution.

The eddy shedding frequencies of all grids were very distinct and as expected (Ref Eq. 1 and Fig. 1) for PSD plots of jet exit velocities less than 90 m/s. As the jet exit velocity was increased from this

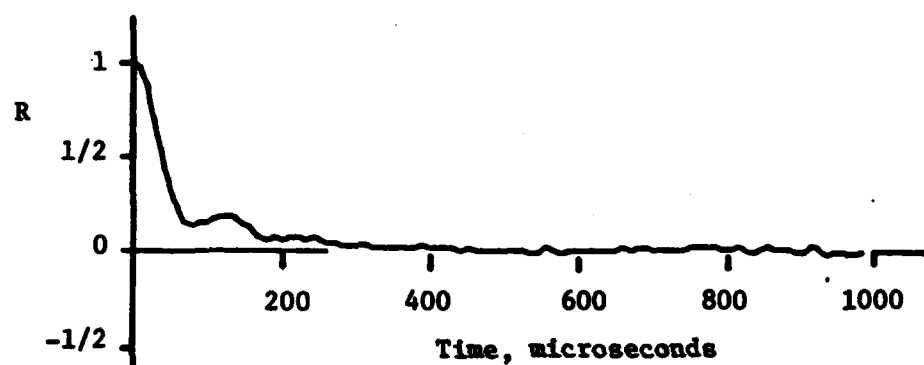
nearly incompressible flow velocity to 200 m/s, the increased shedding frequencies of the smaller diameter rod grids (48, 20 and 10) caused the afore-mentioned mechanical resonances of the anemometer hot film. Also of interest was the increase of turbulence intensity, $\overline{(\rho u)'} / \overline{\rho u}$, behind each particular rod grid as jet exit velocity increased.

At a jet exit Mach number of .6 for grids 2 to 5, the characteristic eddy shedding frequency was most evident at 3 to 4 1/2 diameters downstream of the rods and at a 3 to 1 1/2 diameters lateral or Y direction (Ref Fig. 5) displacement from the rods' axial centerlines. Closer to the rods or further downstream, the autocorrelation and PSD plots became more characteristic of isotropic turbulence. A comparison of representative autocorrelation and PSD plots of data at 2, 1 and 0 diameters lateral offset and 3 diameters downstream of grid 2, Figs. 13 and 14, with similar idealized plots for a strongly periodic flow and isotropic turbulence (see Figs. 3 and 4) indicates this trend.

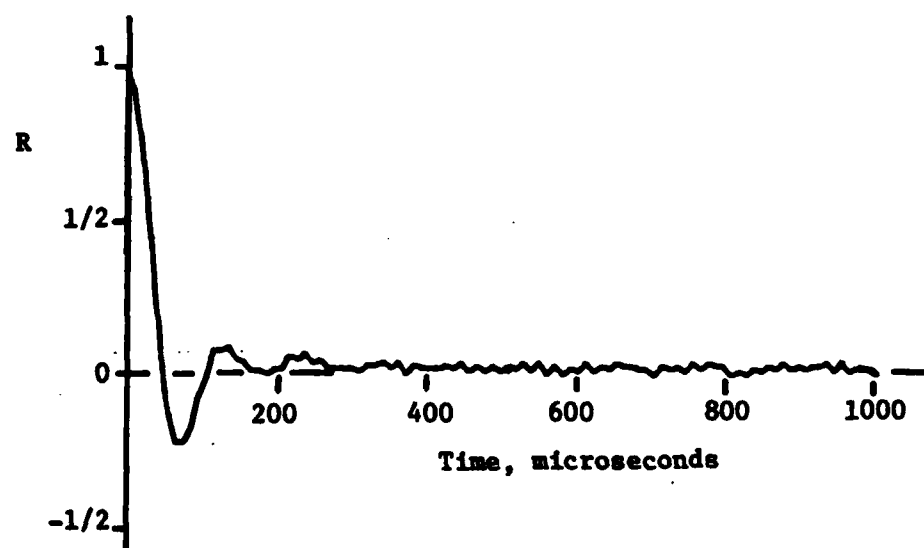
Turbulence intensity decreased directly behind the rods with distance downstream, but increased for the 3 diameters lateral offset position (centerline between rods), approaching a uniform value for all lateral locations at 12 to 15 diameters downstream of the rods. The reverse trend was true for mean velocity, \bar{u} , with \bar{u} very low directly behind rods but characteristic of the theoretical jet exit velocity at 3 diameters lateral offset. Mean velocity approached a uniform value downstream. For the same relative measurement location behind different rod grids, turbulence intensity decreased with smaller rod size while mean velocity recovered to a higher uniform value at 12 to 15 diameters downstream for these smaller rod sizes.



A. 0 Diameters Offset

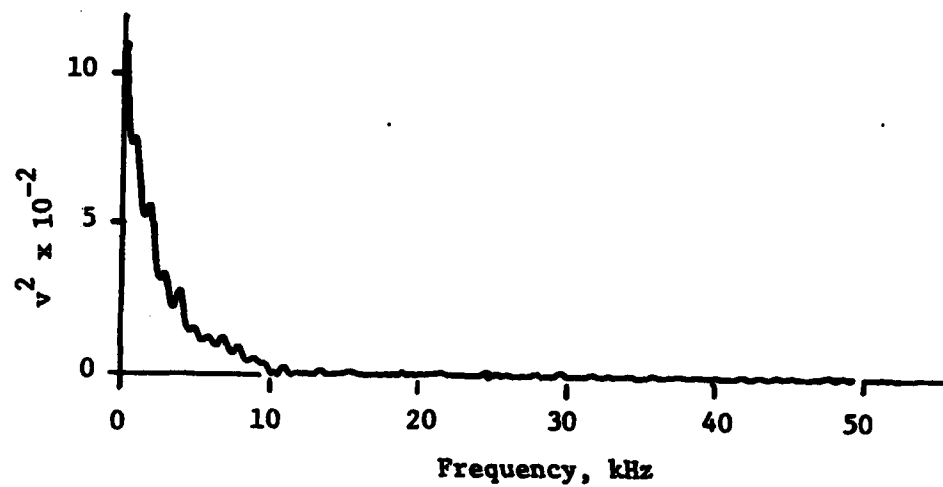


B. 1 Diameter Offset

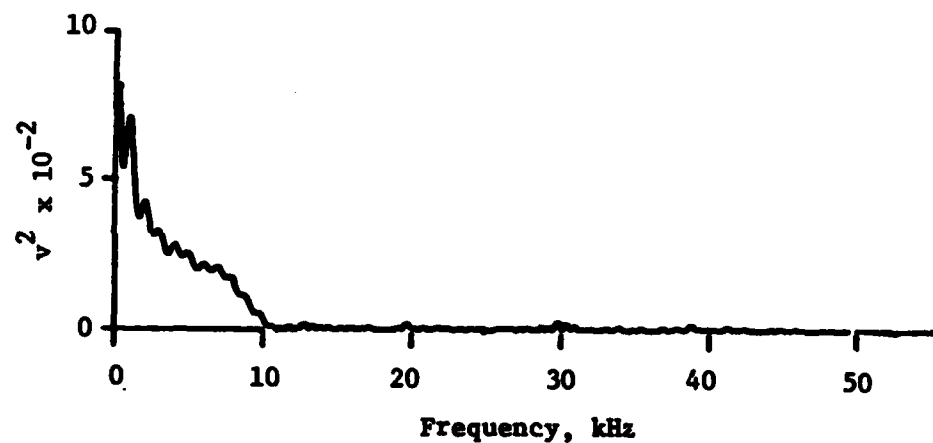


C. 2 Diameters Offset

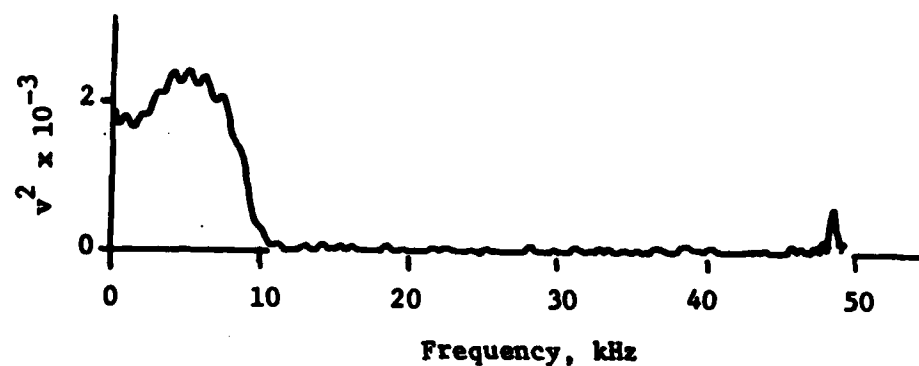
Figure 13. Grid 2 Mass Flux Autocorrelation Plots for Three Lateral Offsets at 3 Rod Diameters Downstream



A. 0 Diameters Offset



B. 1 Diameter Offset



C. 2 Diameters Offset

Figure 14. Grid 2 Mass Flux Power Spectral Density Plots for Three Lateral Offsets at 3 Rod Diameters Downstream

Turbulence intensity increased from a few percent at the 3 diameters lateral location to 25-30% at the 1 1/2 diameters lateral offset point and become several times larger closer in to the rods for traverses 3 diameters downstream of the grids. At the 1 1/2 diameters lateral offset point, turbulence intensity was so large it no longer was an effective measure of turbulence in the classical sense (Ref 15: 39-42).

The application of Taylor's hypothesis (Ref 15: 36-42) to autocorrelation plots of low turbulence data for several representative grids produced characteristic mass flux and pressure eddy lengths two-thirds to one-half that of the actual density eddy length measured at the same flow field location in the schlieren photographs. This result implies the essential correctness of Taylor's hypothesis and the integral scale of the correlation function for highly periodic flows.

Nature of the Near Field Flow

The schlieren photographs at $M = .6$ provided useful data for all seven grid flows. Figs. 15, 16 and 17 are representative schlieren photographs for grids 2, 10 and 48. In general, the density eddies for all grids grew from infinitesimal size at the rod flow separation point to about three times the size of the rod diameter at approximately 9 diameters downstream. Overlapping of rod eddy wakes was very evident at this location. It was not clear whether eddies were alternately shed from a particular rod or alternated from two adjacent rods, although there appeared to be some alternate shedding for single rods on grids 10, 20 and 48. Also, the eddy wakes of the larger rod grids (see Figs. 15 and 16) diverged while those of the smallest rod grids appeared to trail directly behind the rods in a manner characteristic



Figure 15. Schlieren Photograph of Grid 2 Periodic Flow at $M = .6$

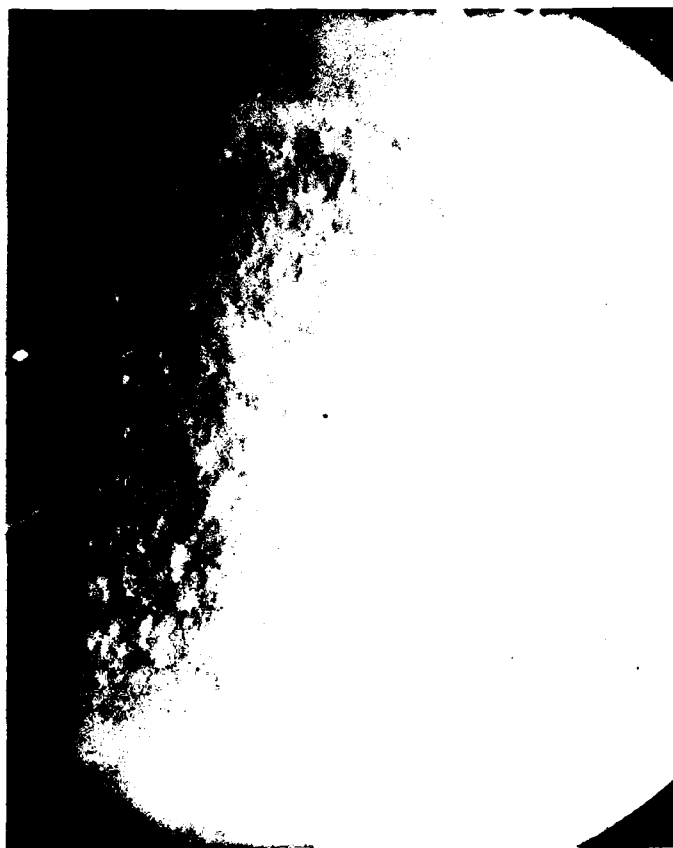


Figure 16. Schlieren Photograph of Grid 10 Periodic Flow at $M = .6$

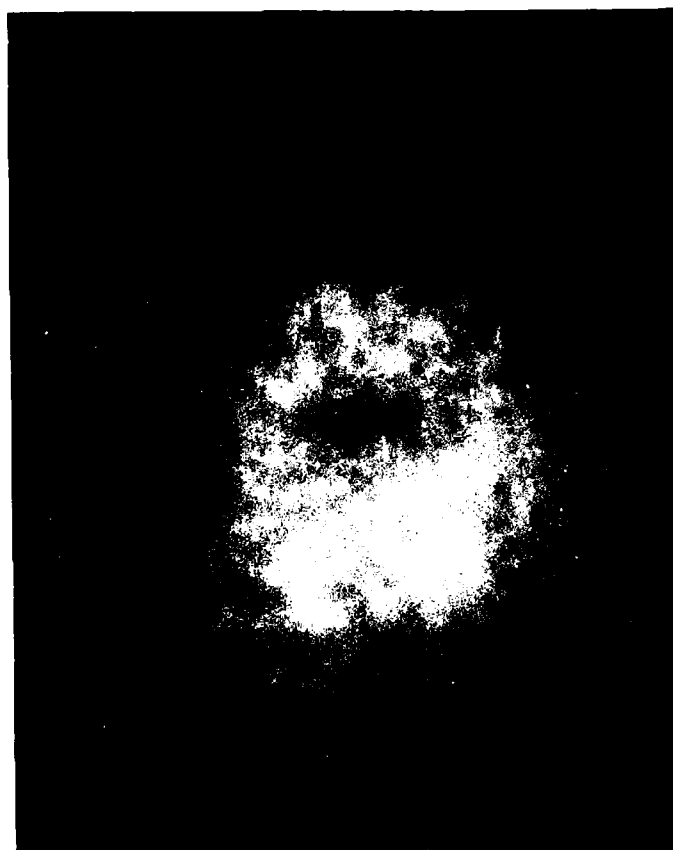


Figure 17. Schlieren Photograph of Grid 48 Periodic Flow at $M = .6$

of a cylinder in a flow duct (see Fig. 2). A further difference was the variation in the eddy wake trailing angles for grid 2 and the flow duct cylinder under almost identical test conditions of Mach number and Re_D (see Table I and Fig. 2). One explanation might be the unconstrained nature of the flow departing the free jet as opposed to the fixed flow boundaries of the duct.

At $2\frac{1}{2}$ to $3\frac{1}{2}$ rod diameters downstream and at a $1\frac{1}{2}$ to 2 diameter offset from the rod centerline the density eddy length was the same size as the rod diameter. A check of eddy shedding frequency was performed for each flow field by deriving an average eddy length from the three or four eddies closest to the rod, assuming the mean velocity was 200 m/s and using the appropriate Strouhal coefficient from Table I as parameters for Eq. 1. Shedding frequencies determined by this approximation were within 10% of the theoretical shedding frequency for all grids except 48. A meaningful frequency could not be determined from the grid 48 photographs due to difficulty in resolving eddy length (Ref Fig. 17). The schlieren photographs were a valuable confirmation and expansion of the anemometer and pressure probe results.

Significance of Beam Degradation

The periodic flow fields significantly affected the laser beam intensity and spot shape. Table III is a summary of beam average peak intensity degradation and variation in beam size. It may be used in conjunction with Tables I and II for this discussion of results.

Over the short 2.5 cm downstream distance between test locations 1 and 3, the influence of the free jet itself, without any grids attached, changed dramatically. The contribution of the free jet

TABLE III

Results of Beam Degradation Measurements

Test Location	Grid Number	.458 micron wavelength			.515 micron wavelength			Beam Spot Shape
		Note 1	Note 2	Note 3	Note 1	Note 2	Note 3	
1	48	91	78	86	90	69	77	slight broadening
	20	91	13	15	90	8	9	Z axis spread, 3 spots
	10	91	12	13	90	11	12	X axis shift, broadening
	5	*	*	*	90	19	21	X axis broadening
2	20	*	*	*	53	15	29	Z axis spread, 2 spots
	10	*	*	*	53	7	13	Z axis spread, 2 spots
	5	67	13	20	53	6	11	general broadening
	4	67	9	13	53	10	18	broadening, X axis trend
3	48	*	*	*	16**	24	**	same as jet-only flow
	10	*	*	*	16**	20	**	broadening, Z axis trend
	3	32	21	64	16**	15	**	horizontal broadening
	2	32	22	67	16**	22	**	more horizontal broadening

Note 1: Jet-only/no-flow Strehl ratio, I-measured beam intensity/I-reference intensity (either flow or jet-only beam intensity), percent

Note 2: Strehl ratio based on no flow, percent

Note 3: Strehl ratio based on jet-only flow, percent

* No test at this point

** Jet-only flow intensity believed to be in error

alone was in the form of a flow shearing zone. The jet core flow interacted with the still air in the test cell to cause a zone of turbulent shear flow at the boundaries between the jet exit air and the test cell air. The zone grew with distance downstream as progressively more jet flow energy was converted to turbulence due to viscous interactions with the test cell air. This shearing zone had little effect at the jet exit but just 2.5 cm downstream its turbulence intensity and bandwidths were such that beam intensity was degraded by two-thirds. At the 2.5 cm location the grids caused some additional beam intensity decay and shape reconfiguration but this additive effect was significantly less than that of the jet-only shearing layers at this location.

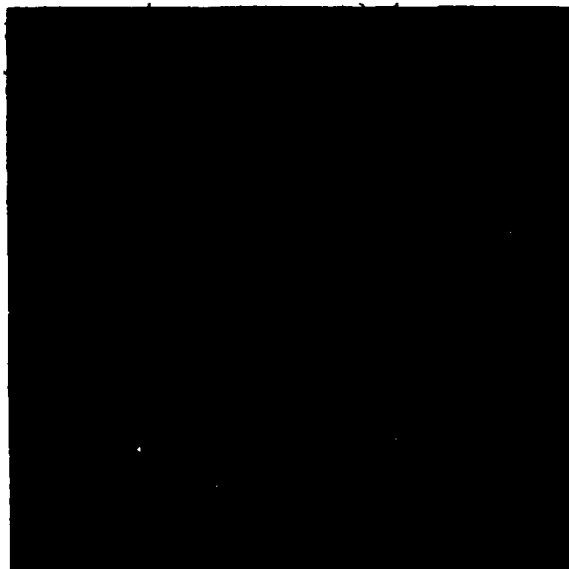
The most significant beam degradation occurred at test location 1. It was not clear whether this was due to eddy passage frequency, density eddy size or the great number and intensities of the eddies caused by the many rods on grids 48, 20 and 10. It was interesting to note that the laser beam Y axis was 23 diameters downstream of grid 48 and covered 21 diameters of area so it was subjected to a wide range of eddies and mixed eddies. The wider "turbulence" bandwidth of grid 48 produced far less beam degradation than the other two grids. Grids 10 and 20 seemed to have the same effect on peak beam intensity but affected the beam shape differently. Schlieren photographs, Table II and Table I indicate that the two grids generated roughly the same size eddy at their respective beam propagation locations and grid 20 had double the shedding frequency of grid 10. Grid 20 may have produced a harmonic of the grid 10 effect. However, it may be seen

from Table III and Figs. 18 and 19, that grid 10 steered the beam in the X direction while grid 20 unexplicably caused the beam to spread in the Z direction. This effect was actually transmitted to the microscope objective and was proven by inserting an index card in front of the objective to see the vertical spreading of the beam focal point.

At test location 2, the impact of grid 20 on the beam was weaker due to eddy mixing, while that of grids 10, 5 and 4 was strong. While grid 20 produced less Z axis spread in beam shape than at test location 1, grid 10 assumed this same characteristic in a departure from its influence at the previous test location. The effect can be seen in Fig. 20. Grids 5 and 4, however, caused beam spread in the horizontal or X direction, as depicted for grid 5 in Fig. 21.

Test location 3 produced a variety of grid effects. At this location, the laser beam was propagated a relative distance of 97 rod diameters downstream of grid 48 where the turbulence was presumed to be of a generalized nature. In fact, the grid appeared to have no significant influence since photographs of the grid 48 and jet-only flow beam intensities appeared identical. Grids 10, 3 and 2 had a progressive effect on the beam degradation caused by the jet shearing action with the test cell air. The jet-only shearing flow broadened the laser beam in the Z direction while the successive addition of grids 10, 3 and 2 caused the beam to become more horizontally broadened in the X direction. Table III and Figs. 22 to 25 indicate the additional beam decay caused by adding the grids and the intriguing effect of the beam shape rearrangement.

The general trends of the beam degradation due to the various flows were well supported by the pseudo-quantitative data derived from the



A. View of X-Z Plane



B. View of
X-Y (Intensity)-
Z Planes

Figure 18. Grid 20 Laser Beam Vertical Broadening
at Test Location 1

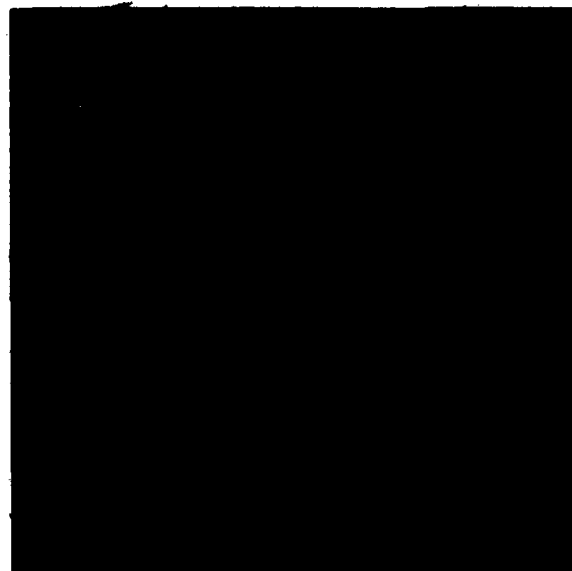


A. View of X-Z Plane

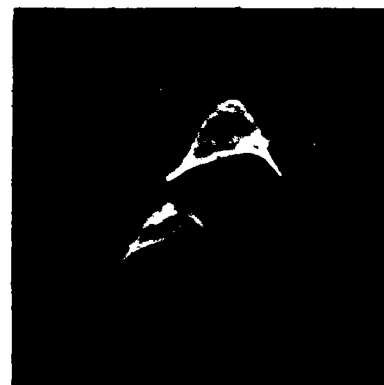


B. View of
X-Y (Intensity)-
Z Planes

Figure 19. Grid 10 Laser Beam Steering
at Test Location 1



A. View of X-Z Plane



B. View of
X-Y (Intensity)-
Z Planes

Figure 20. Grid 10 Laser Beam Vertical Broadening
at Test Location 2



A. View of X-Z Plane



B. View of
X-Y (Intensity)-
Z Planes

Figure 21. Grid 5 Laser Beam Horizontal Broadening
at Test Location 2



A. View of X-Z Plane



B. View of
X-Y (Intensity)-
Z Planes

Figure 22. Jet Shearing Flow Laser Beam Vertical
Broadening at Test Location 3

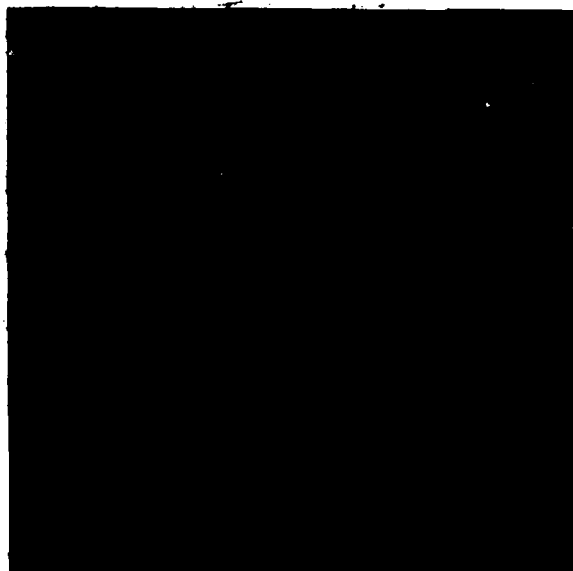


A. View of X-Z Plane



B. View of
X-Y (Intensity)-
Z Planes

Figure 23. Grid 10 Laser Beam Broadening
at Test Location 3

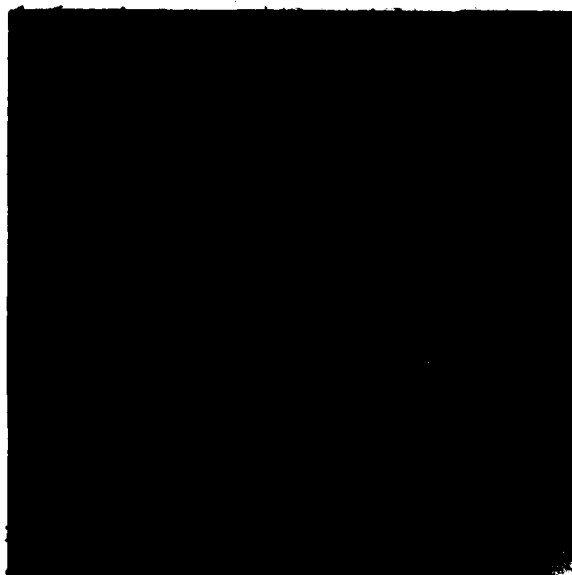


A. View of X-Z Plane



B. View of
X-Y (Intensity)-
Z Planes

Figure 24. Grid 3 Laser Beam Horizontal Broadening
at Test Location 3



A. View of X-Z Plane



B. View of
X-Y (Intensity)-
Z Planes

Figure 25. Grid 2 Laser Beam Horizontal Broadening
at Test Location 3

beam intensity photographs. The careful experimental procedure described in Section IV reduced beam intensity measurement error to less than 10%. The data was almost accurate enough to draw quantitative conclusions. For example, it appeared that the jet-only shearing flow caused more beam degradation of the .515 micron laser wavelength than of the .458 micron wavelength. Because quantitative conclusions of this nature could not be confirmed and since beam degradation due to jet-only shearing interaction with the test cell air increased so rapidly with distance downstream, there was no attempt to correlate grid rod size or laser wavelength to beam degradation.

Anemometer Limitations

All seven of the periodic flow fields caused 22, 45 to 54, 87 to 90, 102 and 210 kHz anemometer signals of large magnitude that biased all mass flux data as well as the autocorrelation and power spectral density plots. The magnitude of these signals was so large that as much as 92% of the fluctuating mass flux energy was due to them. Rod grids 10, 20 and 48 tended to enhance the frequency nearest their calculated shedding frequency, e.g., the 102 kHz frequency was dominant when grid 48 was used. A series of tests eliminated many electrical and mechanical sources of noise. Mechanical resonances of the hot film probe were first suspected when the 22 and 45 kHz signals were noted at very low magnitudes during probe calibrations at velocities greater than 90 m/s. The manufacturer confirmed that probe resonances had been reported (Ref 22). The first three natural frequencies of the long slender probe tips were determined by simple calculations to be on the order of 7.5, 47 and 131 kHz or 33, 106 and 169 kHz, depending on the

method used (Ref 23: 325, 338-339). The details of the calculations are contained in Appendix C. Also, limited testing with a DISA anemometer system revealed similar large magnitude signals first occurring at 34.5 kHz. The tests and calculations indicated that the strong periodic flow fields caused by the rod grids excited the hot film probe natural frequencies producing extremely biased data.

In order to test grids 2 to 5, many types of filtering schemes as well as data taping for digitization and filtering were tried. The General Radio filter was selected for its great attenuation of the resonances and accuracy in reproducing the unfiltered data. With this filter installed in the anemometer data measurement system, the system error was attributed as 2% for hot film reproducibility/calibration curve/manometer setting error, 2% filter error and 2% error in the correlator and spectrum display. Thus, the minimum total anemometer error was 6%.

Pressure Probe Limitations

The pressure probes' Helmholtz and organ pipe resonances were accepted as a design limitation so a filter was included in the pressure measurement system to eliminate these resonance biases from the data (see Section III). The other limitation was the probes' resolution. The probes' sense ports were 30 times the diameter of the anemometer hot film so subtleties of the flow were not as apparent in the pressure probes' measurements. Also, the relatively large cross-section of the probe bodies caused upstream pressure disturbances which contributed to data inaccuracies. The total pressure probe provided a much more distinct frequency profile of the flow than the static probe, perhaps

due to fluid eddy breakup and distortion on the probe nose length upstream of the static port. In the absence of probe resonances, the pressure measurement system error was estimated to be 5% for probe reproducibility/calibration curve/manometer setting error, 2% for the filter and 2% for the correlator and spectrum display for a minimum total system error of 9%.

VI. Conclusions

Several conclusions were drawn from the experimental process that included the creation of seven distinct bandwidths of flow field "turbulence", measurement of flow field parameters and propagation of a laser beam at several wavelengths through the flows.

1. Anemometer hot film, pressure probe and schlieren photograph measurements verified that distinct, periodic fluid eddies in the 5 to 130 kHz passage frequency range were generated by rod grids attached to a $M = .6$ free jet. Eddy lengths the size of the grid rod diameter occurred at $2 \frac{1}{2}$ to $3 \frac{1}{2}$ rod diameters downstream of each grid. The eddies grew in size very rapidly and coalesced at 9 to 12 rod diameters downstream to form generalized, non-isotropic turbulence.
2. The effect of the periodic density fluctuations on the laser beam intensity and spot size was most pronounced for the test location closest to the jet exit, where the smallest grid rods were used. A short distance downstream, the predominant effect on beam degradation was due to the jet flow shearing interaction with the still air of the test cell. The largest diameter rod grids at this location caused interesting changes in the beam shape, overlaying the changes due to the jet shearing action. The inherent inaccuracies of the simple beam degradation

measurement system used in this exploratory research did not allow a positive correlation of fluid eddy size and laser wavelength to beam intensity decay.

3. Mechanical resonances of the anemometer hot film and pressure probes, as well as the relatively large sense port area of the probes, limited their usefulness in the extremely periodic, high frequency flow fields. As a result, useful density fluctuation data could not be obtained for future development of a theory for the eddy dependence of laser beam intensity degradation.

VII. Recommendations

The results of this study can be the basis for continuing research with the existing apparatus or as a point of departure for other studies. Several research areas can be recommended as extensions of this study.

1. Obtain correlations of eddy size and frequency to laser wavelength. Use the existing apparatus with the addition of another laser to provide a range of wavelengths from .4 to 10.6 micron. A refined beam analysis system in the form of a digital, three-dimensional image analyzer might allow instantaneous and time-averaged beam intensities, on-line intensity profiles and intensity oscillation frequency measurements.
2. Propagate a laser beam along the axial direction of the fluid vortices. This variation of the first suggested research area could be achieved by aligning the major axis of the jet exit nozzle vertically.
3. Create flow fields with periodic vortices from a series of grids with single rods or with two staggered rows of rods. These two variations would explore the effects of two extremes; one flow of a single set of fluid eddies, the other flow completely saturated with eddies.
4. Create larger fluid eddies with frequencies and sizes within the resolution limits of the anemometer

hot film and pressure probes. A series of larger, internally heated rod grids could be installed in a wind tunnel to enhance density fluctuations at the lower test velocity necessary to remain below the $2 \times 10^5 Re_D$ limit for stable vortex flows.

5. Analytically derive the density fluctuations behind the rod grids. The grid flows could be modelled and investigated through the use of numerical schemes and computational aerodynamics.

Bibliography

1. Gilbert, K. "An Aero-Optics Overview". Unpublished lecture presented to Aero-Optics Symposium, NASA Ames Research Center, Moeffet Field, California. 14-15 August 1979.
2. Sutton, G. W. "Effect of Turbulent Fluctuations in an Optically Active Fluid Medium", AIAA Journal, 7: 1737-1743 (September, 1969).
3. Cudahy, G. F. An Investigation of the Degradation of a Laser Beam by High Intensity Turbulence. PhD Dissertation. Wright-Patterson Air Force Base, Ohio: Air Force Institute of Technology, 1976.
4. Gilbert, K. "Aircraft Aero-Optical Turbulent Boundary-Layer/Shear-Layer Measurements," Laser Digest-Fall 1977: 154-176, AFWL-TR-78-15. Kirtland Air Force Base, New Mexico: Air Force Weapons Laboratory (April 1978).
5. Loehrke, R. I. and Nagib, H. M. "Control of Free Stream Turbulence by Means of Honeycombs: A Balance Between Suppression and Generation", Transaction of the ASME, Journal of Fluids Engineering, 342-353 (September 1976).
6. Jumper, E. J. Personal communication. School of Engineering, Air Force Institute of Technology, Wright-Patterson Air Force, Ohio. January, 1982.
7. Shepard, W. K. Turbulence Measurements in a Plane Free Jet at High Subsonic Velocities. M.S. Thesis. Wright-Patterson Air Force Base, Ohio: Air Force Institute of Technology, December 1974.
8. Kirchner, M. J. Computer Assisted Velocity and Turbulence Measurements in a Plane Free Jet at High Subsonic Velocities. M.S. Thesis. Wright-Patterson Air Force Base, Ohio: Air Force Institute of Technology, December 1981.
9. Roshko, A. "On the Development of Turbulent Wakes from Vortex Streets". Fortieth Annual Report of the NACA: 801-825, NACA TR 1191. U.S. Government Printing Office, 1956.
10. Schlichting, H. Boundary Layer Theory. New York: McGraw-Hill Co., 1979.
11. Wille, R. "Karman Vortex Streets", Advances in Applied Mechanics, Vol VI, edited by G. Kuerti. New York: Academic Press, 1960.

12. Rose, W. C. et al. Near Field Aerodynamics and Optical Propagation Characteristics of a Large-Scale Turret Model, AFWL-TR-81-28. Kirtland Air Force Base, New Mexico: Air Force Weapons Laboratory, February 1982.
13. Horstman, C. C. and Rose, W. C. "Hot Wire Anemometry in Transonic Flow", AIAA Journal, 15: 395-401 (March 1977).
14. Bendat, J. S. and Piersol, A. G. Measurement and Analysis of Random Data. New York: Wiley and Sons, 1966.
15. Hinze, J. O. Turbulence. New York: McGraw-Hill Co., 1959.
16. Otten, L. J. and Van Kuren, J. T. "Artificial Thickening of Transonic Boundary Layers," AIAA 14th Aerospace Science Meeting. AIAA Paper 76-51. Washington, D. C., 1976.
17. Shapiro, A. H., The Dynamics and Thermodynamics of Compressible Fluid Flow, Vol 1. New York: Wiley and Sons, 1953.
18. Henney, K. and Dudley, B. Handbook of Photography. New York: McGraw-Hill Co., 1939.
19. Arent, L. E. Experimental Investigation of Flow Behind Staggered Cylinders: M.S. Thesis. Wright-Patterson Air Force Base, Ohio: Air Force Institute of Technology, December 1971.
20. Harris, C. M. (Editor). Handbook of Noise Control, Sec 21. New York: McGraw-Hill Co., 1957.
21. Beckwith, T. G. and Buck, N. L. Mechanical Measurements. Reading, Massachusetts: Addison-Wesley Co., 1961.
22. Kolbeck, W. Telephone communication. Thermo-Systems, Inc., St. Paul, Minnesota. August 1982.
23. Timoshenko, S. Vibration Problems in Engineering: Princeton: Van Nostrand Co., 1955.

Appendix A

Derivation of Fluctuating Density from

Mass Flux and Pressure Measurements

The equation of state can be expressed in terms of quantities that can be measured in a flow by the hot wire anemometer and pressure probes. (Ref 12: 20-23). The first step is to derive the differential form of the equation of state:

$$P = \rho RT \quad (A1)$$

$$dP = RT d\rho + \rho T dR + \rho R dT \quad (A2)$$

$$\frac{dP}{\rho RT} = \frac{d\rho}{\rho} + \frac{dT}{T} \quad (A3)$$

$$\frac{P'}{\bar{P}} = \frac{\rho'}{\bar{\rho}} + \frac{T'}{\bar{T}} \quad (A4)$$

where P' = fluctuating static pressure
 \bar{P} = mean flow static pressure
 ρ' = fluctuating density
 $\bar{\rho}$ = mean flow density
 T' = fluctuating static temperature
 \bar{T} = mean flow static temperature

In a similar manner the isentropic relationship

$$T_t = T \left(1 + \frac{K-1}{2} M^2 \right) = T + \frac{u^2}{2C_p} \quad (A5)$$

can be rearranged to differential form:

$$\left(1 + \frac{K-1}{2} M^2 \right) \frac{T'_t}{T_t} - [(K-1) M^2] \frac{u'}{u} = \frac{T'}{\bar{T}} \quad (A6)$$

Define:

$$D \equiv 1 + \frac{K-1}{2} M^2$$

$$E \equiv (K-1) M^2$$

Substituting from Eq. A6 for T'/\bar{T} in Eq. A4:

$$\frac{P'}{\bar{P}} - \frac{\rho'}{\bar{\rho}} + (E) \frac{u'}{\bar{u}} = (D) \frac{T'_t}{\bar{T}_t} \quad (A7)$$

Adding and subtracting $(E) \frac{\rho'}{\bar{\rho}}$ on the left hand side of Eq. A7:

$$\frac{P'}{\bar{P}} - (1+E) \frac{\rho'}{\bar{\rho}} + E \frac{(\rho u)'}{\bar{\rho} \bar{u}} = D \frac{T'_t}{\bar{T}_t} \quad (A8)$$

Each of the mean and fluctuating quantities in Eq. A8 can be directly measured. If total temperature fluctuations are negligible then Eq. A8 reduces to:

$$\frac{P'}{\bar{P}} + E \frac{(\rho u)'}{\bar{\rho} \bar{u}} = (1 + E) \frac{\rho'}{\bar{\rho}} \quad (A9)$$

Define:

$$F = (1 + E)$$

Since mass flux, $(\rho u)'$, and pressure cannot be measured at the same location simultaneously, Eq. A9 is time-averaged to produce

$$F^2 \frac{\overline{(\rho')^2}}{\bar{\rho}^2} = \frac{\overline{(P')^2}}{\bar{P}^2} + 2 E R_{P \rho u} \frac{\langle (\rho u)' \rangle \langle P' \rangle}{(\bar{\rho} u) (\bar{P})} + E^2 \frac{\overline{[(\rho u)']^2}}{(\bar{\rho} u)^2} \quad (A10)$$

where

$\langle (\rho u)' \rangle$ = root mean square of fluctuating mass flux

$\langle P' \rangle$ = root mean square of fluctuating static pressure

$R_{P \rho u}$ = cross correlation coefficient between $(\rho u)'$ and P'

Several research efforts have revealed that $R_{p \rho u}$ is negligible in turbulent boundary layers (Ref 12: 23). It is not clear whether $R_{p \rho u}$ is negligible for a strongly periodic flow field. If it is assumed to be negligible, Eq. A10 becomes:

$$[1+(K-1)M^2] \frac{\overline{(\rho')^2}}{\bar{\rho}^2} = \frac{\overline{(P')^2}}{\bar{P}^2} + [(K-1)M^2] \frac{\overline{(\rho u')^2}}{(\bar{\rho u})^2} \quad (A11)$$

The mean and fluctuating flow parameters in Eq. A11 can be measured and mean density calculated from the equation of state. With these values, fluctuating density can be determined at flow measurement locations.

Appendix B

Relationship of Measured Density to Beam Intensity

The density data provided by densitometer analysis of photographs of the far-field, degraded laser beam can be directly related to beam intensity. Assume the semi-opaque receiver plate transmits a known percentage, I , of the laser beam intensity. The spot intensity perceived by the film surface will generally be a function of spot size, wavelength λ , and time of exposure in what is known as the exposure, E :

$$E = \int_{\text{Area}} \int_{\lambda_{\text{lower}}}^{\lambda_{\text{upper}}} \int_0^T I(\lambda, x, z, t) dt d\lambda dA \quad (\text{B1})$$

Considering only the intensity at a discrete point at the single wavelength of the laser light, Eq. B1 simplifies to:

$$E = \int_0^T I(t) dt \quad (\text{B2})$$

Furthermore, if the laser intensity is constant with time, (Ref 18: 162,270) then:

$$E = It \quad (\text{B3})$$

The exposure sensitivity of a particular photographic surface is evident in what is known as the film's characteristic curve. The curve is depicted in Fig. 26 and is a plot of film density, d , versus \log_{10} of exposure. Below a certain exposure level, E_0 , the film negative is insensitive and density remains unchanged. Increased exposure above E_0 increases the negative density.

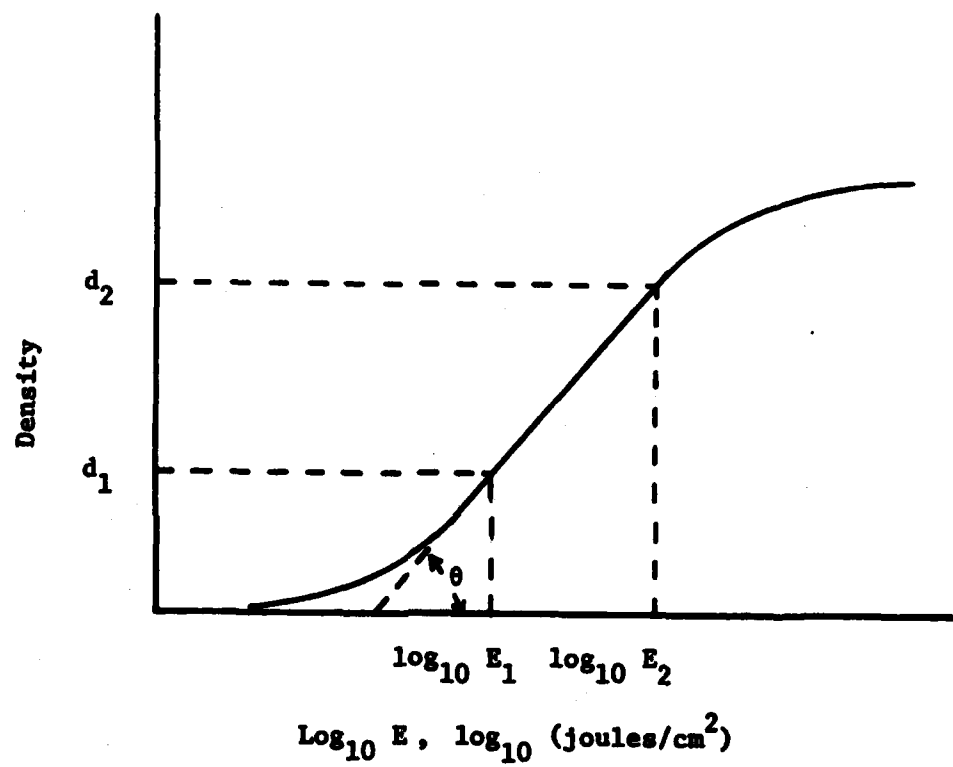


Figure 26. Characteristic Curve of Film Response

Density, d , is related to exposure in the linear portion of the curve by the relationship (Ref 18:179-180):

$$\gamma = \tan \theta = \frac{d_2 - d_1}{\log_{10} E_2 - \log_{10} E_1} = \frac{d_2 - d_1}{\log_{10} (E_2/E_1)} \quad (B4)$$

If γ , the slope of the characteristic curve, is known and d_2 and d_1 are measured by densitometer for undisturbed and degraded beams, respectively, then the exposure ratio is:

$$\frac{E_1}{E_2} = 10^{-\frac{(d_2 - d_1)}{\gamma}} \quad (B5)$$

If, from Eq. B3, the exposure time for each photograph is constant:

$$\frac{I_1}{I_2} = 10^{-\frac{(d_2 - d_1)}{\gamma}} \quad (B6)$$

Equation B6 is the relationship for deducing a Strehl ratio of disturbed and undisturbed beam intensities from photographic negatives of the two beams.

If γ is not known, it can be determined empirically for a particular laser wavelength interaction with the film negative. Two negatives are exposed for different periods of time to an undisturbed laser beam. Since the beam intensity, I , will be equal for each negatives, the exposure ratio will reduce to an exposure time ratio:

$$\frac{E_1}{E_2} = \frac{It_1}{It_2} = \frac{t_1}{t_2} \quad (B7)$$

If t_1 was one-half that of t_2 , then Eq. B5 becomes:

$$\frac{t_1}{t_2} = \frac{1}{2} = 10^{-\frac{(d_2 - d_1)}{\gamma}} \quad (B8)$$

$$\log_{10} \frac{1}{2} = \frac{-(d_2 - d_1)}{\gamma} \quad (B9)$$

$$\gamma = \frac{d_2 - d_1}{.301} \quad (B10)$$

Since the peak density of the beam can be measured on the negatives, γ can be determined.

Appendix C

Hot Film Mechanical Resonances Calculations

A precise derivation of the system natural frequency for the two long, semi-tapered pins that support and present the anemometer hot film element to the flow would be a complex model of multiply-pinned beams. A simple calculation of the natural frequencies assumes the short quartz film to be relatively stiff and the semi-tapered pins as beams of constant cross-section. With this approach, the analysis becomes one of a beam (semi-tapered pin) with one end built into a wall and the other end free or supported (by the combination of the quartz film and other pin). The natural frequencies of each are easily calculated provided certain properties of the beam are known or derived (Ref 23: 325, 338-339):

E_m -modulus of elasticity, $2.11 \times 10^6 \frac{\text{kg}}{\text{cm}^2}$ for stainless steel

I_m -moment of inertia, $\frac{\pi r^4}{4} = \frac{\pi (.0211)^4}{4} \text{ cm}^4$ for a circular cylinder

A-cross-sectional area, $\pi r^2 = \pi (.0211)^2 \text{ cm}^2$

l-length, .635 cm

w-specific weight, $7.9 \times 10^{-3} \frac{\text{kg}}{\text{cm}^3}$

g-acceleration due to gravity, $980 \frac{\text{cm}}{\text{sec}^2}$

Using these properties the first three natural frequencies of a con-

stant cross-section area beam with one end built in, one end free are

$$f_1 = \frac{a (K_1)^2}{2\pi} \quad (C1)$$

where

$$a = \left(\frac{E I_m g}{A w} \right)^{1/2} \quad (C2)$$

$$K_1 = \frac{1.875}{1} \quad (C3)$$

$$K_2 = \frac{4.694}{1} \quad (C4)$$

$$K_3 = \frac{17.855}{1} \quad (C5)$$

The first three natural frequencies of the free-end beam, using Eqs. C1, C2 and C3 to C5 as appropriate, are 7.5, 47 and 131 kHz. The first three natural frequencies of a beam with one-end built in, the other end supported are calculated using Eqs. C1 and C2 with:

$$K_1 = \frac{3.927}{1} \quad (C6)$$

$$K_2 = \frac{7.069}{1} \quad (C7)$$

$$K_3 = \frac{10.210}{1} \quad (C8)$$

The first three natural frequencies calculated with this method are 33, 106 and 169 kHz.

Vita

Craig P. Weston was born 27 February 1950 in Tokyo, Japan. He graduated from Cordova High School, Rancho Cordova, California in 1968 and entered the United States Air Force Academy. He received his Bachelor of Science Degree in Engineering Mechanics and a commission in the USAF upon graduation from the Academy in 1972. He served a tour as a Mechanical Engineer at the Armament Development and Test Center, Eglin Air Force Base. During a subsequent assignment to the Air Force Weapons Laboratory, Kirtland Air Force Base, he first served as a Laser Weapon System Engineer and then as Chief, Airborne Laser Laboratory Gas Dynamic Laser Section. He entered the Graduate Aeronautical Engineering Program at the Air Force Institute of Technology in June 1981.

Permanent Address: 2616 Benny Way
Rancho Cordova, California 95670

UNCLASSIFIED

SECURITY CLASSIFICATION OF THIS PAGE (When Data Entered)

REPORT DOCUMENTATION PAGE		READ INSTRUCTIONS BEFORE COMPLETING FORM
1. REPORT NUMBER AFIT/GAE/AA/82D-32	2. GOVT ACCESSION NO. AD A224736	3. RECIPIENT'S CATALOG NUMBER
4. TITLE (and Subtitle) INFLUENCE OF PERIODIC COMPRESSIBLE VORTICES ON LASER BEAM INTENSITY		5. TYPE OF REPORT & PERIOD COVERED MS Thesis
7. AUTHOR(s) Craig P. Weston Captain USAF		6. PERFORMING ORG. REPORT NUMBER
9. PERFORMING ORGANIZATION NAME AND ADDRESS Air Force Institute of Technology (AFIT-EN) Wright-Patterson AFB, Ohio 45433		8. CONTRACT OR GRANT NUMBER(s)
11. CONTROLLING OFFICE NAME AND ADDRESS Air Force Institute of Technology (AFIT-ENY) Wright-Patterson AFB, Ohio 45433		10. PROGRAM ELEMENT, PROJECT, TASK AREA & WORK UNIT NUMBERS
14. MONITORING AGENCY NAME & ADDRESS (if different from Controlling Office)		12. REPORT DATE December, 1982
		13. NUMBER OF PAGES 81
		15. SECURITY CLASS. (of this report) Unclassified
		15a. DECLASSIFICATION/DOWNGRADING SCHEDULE
16. DISTRIBUTION STATEMENT (of this Report) Approved for public release; distribution unlimited.		
17. DISTRIBUTION STATEMENT (of the abstract entered in Block 20, if different from Report)		
<p>Approved for public release: IAW AFR 190-17.</p> <p><i>Lynd E. Wolaver</i> LYND E. WOLAVER Dean for Research and Professional Development Air Force Institute of Technology (ATC) Wright-Patterson AFB OH 45433</p> <p>Approved for public release; IAW AFR 190-17. Frederic C. Lynch, Major, USAF Director of Public Affairs</p> <p>19 JAN 1983</p>		
18. SUPPLEMENTARY NOTES		
19. KEY WORDS (Continue on reverse side if necessary and identify by block number)		
laser propagation free jet laser beam degradation vortex generation refractive index perturbation cylinder shedding periodic density fluctuation hot wire anemometer narrow band flow disturbance		
20. ABSTRACT (Continue on reverse side if necessary and identify by block number)		
The effect of narrow-band, vortex-induced density fluctuations on the beam quality of a laser propagated through the fluctuating flow was explored. The vortex flows were created by cylindrical rods placed at the exit plane of a 1 cm by 10 cm rectangular free jet issuing air at $M = .6$. Reynolds number based on rod diameter varied from 4.6×10^3 to 1.1×10^5 . Mean and fluctuating mass flux, total pressure and static pressure time histories of the flows were measured in order to derive fluid eddy passage frequency, eddy length and periodic density fluctuation data. Schlieren photographs were obtained for further assessment of		

DD FORM 1 JAN 73 1473

EDITION OF 1 NOV 65 IS OBSOLETE

UNCLASSIFIED

SECURITY CLASSIFICATION OF THIS PAGE (When Data Entered)

UNCLASSIFIED

SECURITY CLASSIFICATION OF THIS PAGE(When Data Entered)

20. (continued)

the flow fields. A nominal 1 mW laser beam was propagated at two wavelengths transversely through the periodic portion of each flow. The far field beam cross-section was analyzed to determine beam intensity degradation. A Strehl ratio for each flow field was deduced from pseudo-quantitative data. A hot film anemometer and pressure probes provided limited mass flux and pressure time history data due to mechanical resonances caused by the high frequencies and strength of eddy generation. The schlieren photographs confirmed that distinct, periodic fluid eddies existed for at least nine rod diameters downstream of the jet exit. All of the rod grids produced significant beam degradation but each grid affected the beam shape differently.

UNCLASSIFIED

SECURITY CLASSIFICATION OF THIS PAGE(When Data Entered)

END

FILMED

3-83

DTIC